Model Analysis and Design of the Control Strategy for the Bidirectional Resonant DAB Converter

Pengyu Jia, *Member, IEEE*, Yiheng Zhang, *Student Member, IEEE*, Mingjun Liu, *Student Member, IEEE*, and Yimei Xing, *Student Member, IEEE*

***Abstract*—The model of the *CLLC* resonant dual active bridge (DAB) converter, which adopts the switching frequency and the single phase shift angle as the control variables, is built and analyzed in this article. The soft-switching region is given and a symmetrical circuit parameter design method considering bidirectional wide voltage variation range is proposed. Correspondingly, a control strategy is proposed. With the proposed tunable linear function ($\varphi = \mathrm{K_m} \times f_\mathrm{n} + \mathrm{B_m}$) between the normalized frequency f_n and the phase shift angle φ, a good balance between the switching frequency range, efficiency, bidirectional gain range, and the load range can be made. The proposed control strategy employs the same 0.5 duty cycles for both the primary and secondary side switches to achieve a natural synchronous rectification. Besides, a feedforward control algorithm is provided, which uses a curve fitting method to obtain the approximate value of the control variables and can improve the dynamic response. The correctness of the theoretical analysis and the feasibility of the proposed method are verified by a 1 kW bidirectional resonant DAB experimental prototype, where the switching frequency only changes 18.84% within a load variation from 20% to 100% under a bidirectional normalized gain range of 2.25.**

***Index Terms*—Bidirectional converter, *CLLC* resonant converter, dual active bridge, soft switching, wide voltage range.**

I. Introduction

With the development of new energy industry, the research of isolated bidirectional dc–dc converter has become an important field in power electronics, which have been widely applied in electric vehicles [1], uninterruptible power supplies [2], aerospace power systems [3], and renewable energy systems [4], [5], [6].

LLC resonant converter is a good solution as a unidirectional power supply with variable frequency (VF) control since it can achieve the soft-switching over the full load range and voltage range [7], [8], [9], [10]. However, its voltage range is limited when the power flows backward: the magnetizing inductance is always clamped by the input voltage so the resonant tank is equivalent to a *LC* series resonant tank. As a result, the step-up capability is lost [11]. In order to solve this problem, an auxiliary inductor can be placed in the primary side [see Fig. 1(a)] to form a symmetric resonant tank [12], [13]. Therefore, the converter shows the similar characteristics like the *LLC* converter in any power flow direction. However, it is worth noting that it suffers the risk of the core saturation since there is no block capacitor in the secondary-side winding and the auxiliary inductor branch.

Another *LC* resonant branch can be set in the secondary side to form a *CLLC* resonant tank, which can also realize the step-up function in any direction [14], [15], [16], [17], [18], [19], [20]. Different from the first scheme, this method does not saturate the core due to the existence of the capacitors C_a, C_b [see Fig. 1(b)]. Moreover, it is proved that the converter can be completely equivalent to the asymmetric *LLC-C* converter, as shown in Fig. 1(c) [20], [21], so the number of resonant

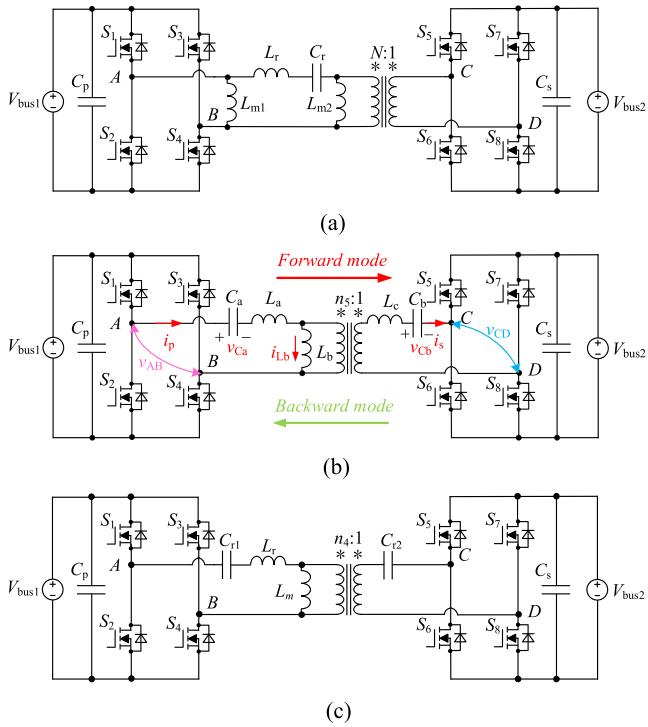

Fig. 1. Three kinds of bidirectional converters derived from the *LLC* converter. (a) *LLC-L* type. (b) *CLLC* type. (c) *LLC-C* type.

Received 8 August 2024; revised 2 November 2024 and 11 January 2025; accepted 15 February 2025. Date of publication 18 February 2025; date of current version 14 April 2025. This work was supported in part by the Beijing Natural Science Foundation under Grant 3232044 and in part by the R&D Program of Beijing Municipal Education Commission under Grant KM202110009011. Recommended for publication by Associate Editor J. Lam. *(Corresponding author: Pengyu Jia.)*

The authors are with the College of Electrical and Control Engineering, North China University of Technology, Beijing 100144, China (e-mail: 08117338@bjtu.edu.cn).

Color versions of one or more figures in this article are available at https://doi.org/10.1109/TPEL.2025.3543718.

Digital Object Identifier 10.1109/TPEL.2025.3543718

inductors can be further reduced in order to improve the power density.

When the body diode of switch is employed as the rectifier stage, the conduction loss of the diode severely limits the efficiency. In order to improve the efficiency, synchronous rectification (SR) is usually applied, such as the hardware detection [22], [23] and the predictive method based on the mathematical model [24], [25], [26], [27]. The hardware detection method usually employs a current transformer to detect the current zero-crossing point so as to generate the driving pulses of the SR switches. This brings extra detection circuit and increases the cost. The predictive SR method needs to online calculate the conduction phase angle for the SR switches based on the converter model. However, the accuracy of the model directly affects SR performance.

Different from [22], [23], [24], [25], [26], [27], several open-loop SR methods are proposed in order to facilitate the implementation. In [28], the conduction time of the secondary-side switch is fixed equal to half of the resonant period ($T_r/2$) so as to decrease the backflow power. In [29], the converter operates with the similar method like [28] when it is operated in step-up mode, but the duty cycles of the primary and secondary side switches exchanged when the converter operates in step-down mode. Due to the constant conduction time for the secondary-side switches, which is set equal to half of the resonant period ($T_r/2$), the situation that current flows through the body-diode of the switch still exists. Therefore, the efficiency is hard to be improved. Liu et al. [30] focused on the condition that the normalized gain varies far away from unity, and proposed that the conduction time for both sides is fixed equal to half the resonant period. However, there still exist the stages in [28], [29], and [30], where the body diode conducts for a long time after the switching transition. So, the diode conduction loss still takes a part of the total loss.

A good solution to eliminate the body-diode conduction loss is that the switches in the same bridge leg are driven complementarily, such as [31], [32], [33], [34], [35], [36], [37], [38], [39], [40], and [41]. This can be also considered as an open-loop SR method. As a result, the current always flows through the channels of the switch instead of the body diodes. In this case, the converter evolves into a resonant dual active bridge (RDAB) converter. In [31], [32], [33], [36], [37], [38], [39], [40], and [41], all the switches adopt 0.5 duty cycles to realize a natural SR and the output can be regulated through the switching frequency and/or the phase shift angles. However, as mentioned above, Jiang et al. [31], Jia et al. [32], [33], and Wu et al. [34] may face the risk of core saturation problems. Huang et al. [35] can be considered as an improvement of [34], where the half-bridge inverter with dc capacitor bridge legs and clamped diodes is applied to avoid the core saturation problem. However, the utilization ratio of the input voltage is decreased to half when compared with the full-bridge inverter. Therefore, with the same power level and input voltage range, the current stress for the switch is doubled. Similar problems of high current stress for the switch also exist in [36]. Twiname et al. [37], Malan et al. [38], Meinagh et al. [39], and Cheng et al. [40] proposed the triple phase shift (TPS) modulation to decrease the reactive power and reduce conduction loss. However, the effect of voltage variation is not taken into account in [37], [38], and [39]. In [41], switching frequency and single phase shift (SPS) angle are both adopted as the control variables. In this way, the secondary-side switch can realize a natural SR to improve the efficiency. However, only open loop experimental results are given but no relationship function between the two control variables is proposed. Meanwhile, the effect of the gain variation is not considered.

The purpose of this article is to provide a bidirectional design reference, which can make a good balance between the frequency range, efficiency, voltage range, and reliability (elimination of core saturation) for the practical realization for engineering. Due to the existence of the resonant capacitors on both sides, *CLLC* RDAB (or a *LLC-C* RDAB, which can be proved equivalent to each other) naturally has the advantage of eliminating the risk of core saturation. Hence, this topology is focused in this article. Due to the lack of the parameter design guidelines and corresponding control strategy for it with VF&SPS control, the model is built and analyzed in this article. The main contribution of this article is summarized as follows.

1) By employing the switching frequency (f_s) and single *phase shift* angle (φ) as the control variables, the mathematical model of CLLC converter [see Fig. 1(b)] is derived. The key step in the parameter design process, which is the determination of the switching frequency range and the selection of the resonant parameters, is derived and described in detail, so as to enlarge the soft-switching range.
2) Based on the model, a VF&SPS control strategy is proposed. The *phase shift* angle (φ) is combined with switching frequency (f_s) by a mathematical linear function, which is with the tunable dummy parameters related to the voltage gain. By this means, the switching frequency variation can be limited to a narrow frequency range while covering a wide bidirectional voltage range, so as to facilitate the design of the transformer. Different from [17], [18], [19], [29], [34], [35], [36], [37], [38], which only consider voltage variation on one side, the proposed method is applicable to the situation where voltage variation exists at both ports of the converter.
3) Based on the model, a feedforward controller is proposed. With a curve fitting method, the feedforward algorithm can be realized by a linear function between frequency (f_n) and the product of gain and quality factor ($M_{gn} \times Q$) instead of the complicated trigonometric function.
4) Under the specification given in Section VI, the circuit parameters of CLLC RDAB and LLC-C RDAB converters are determined as an example. By the experimental verification, it shows a good balance between the efficiency, component numbers, the voltage range, and load range when compared to other existing methods.

II. Analysis of Bidirectional CLLC RDAB Converter

When designing the *CLLC* RDAB converter, as shown in Fig. 1(b), a symmetric design approach is usually adopted to reduce the design complexity, as shown in (1) and (2). By this means, there are only four design freedom degrees for the

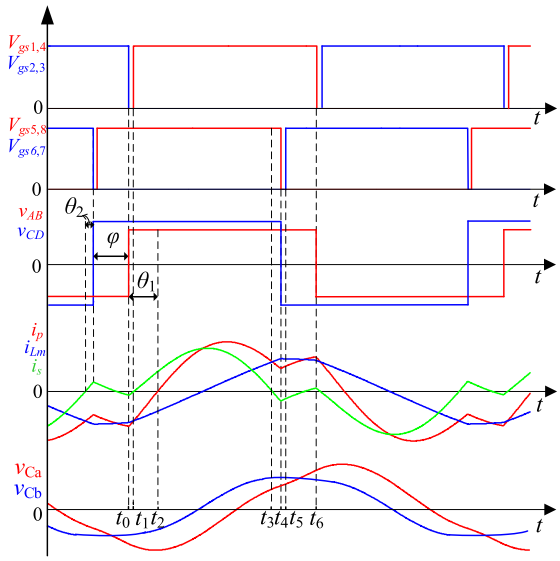

Fig. 2. Key waveforms with VF&SPS control.

parameters, which are L_a, C_a, n_5, and L_b. Here, the subscript "5" of the transformer turns ratio n_5 means that the resonant tank is composed of five components. Correspondingly, the subscript "4" in Fig. 1(c) means there are four resonant elements in the *LLC-C* converter

$$L_a = {n_5}^2 L_c \tag{1}$$

$$C_b = {n_5}^2 C_a. \tag{2}$$

A. Operation Principle

The key waveforms of the *CLLC* resonant converter are shown in Fig. 2. The primary and secondary side switches both adopt 0.5 duty cycles for the driving pulses with the same frequency. The symbol φ ($\varphi \in [0, \pi]$) is defined as the SPS angle between v_{AB} and v_{CD}. The symbol θ_1 denotes the phase angle between v_{AB} and i_p and meanwhile, θ_2 denotes that between v_{CD} and i_s. Considering the symmetric feature of the waveforms, only the operation stages in half of the switching period are analyzed. The equivalent circuits in different operation stages are shown in Fig. 3.

Stage I (t_0-t_1): This stage is the switching *dead time* of the primary side switches. S_2 and S_3 are turned OFF at t_0. In this stage, the current i_p is always negative and i_p charges the *drain-source* capacitance of S_2 and S_3 and meanwhile, discharges that of S_1 and S_4. Then, i_p flows through the body diode of S_1 and S_4 to provide the necessary condition for the ZVS turn-ON for the switches.

Stage II (t_1-t_2): The driving signals of S_1 and S_4 are given at t_1 and a ZVS turn-ON is realized. The direction of i_s changes from negative to positive at t_1.

Stage III (t_2-t_3): During this stage, power flows from primary side to secondary side. The direction of i_p changes from negative to positive at t_2.

Stage IV (t_3-t_4): The direction of i_s changes from positive to negative at t_3. During this stage, S_5 and S_8 still conduct. Therefore, power flows from the secondary side to resonant tank. The circulating current is the necessary condition for S_6 and S_7 to realize ZVS turn-ON.

Stage V (t_4-t_5): This stage is the switching *dead time* of the secondary side switches. S_5 and S_8 are turned OFF at t_4. In this stage, the current i_s is always negative and i_s charges the *drain-source* capacitance of S_5 and S_8 and discharges that of S_6 and S_7. Then, i_s flows though the body diode of S_6 and S_7 to provide the necessary condition for the ZVS turn-ON for the switches.

Stage VI (t_5-t_6): The driving signals of S_6 and S_7 are given at t_5 and a ZVS turn-ON is realized. The converter operates the next half switching period after t_6.

B. Normalized Gain in the Forward and Backward Modes

A mathematical model is necessary to observe the effect of control variables for the converter. The time-domain analysis (TDA) modeling method has a great accuracy by solving the differential equations at a switching period. However, the complete analytic solution is hard to be obtained by TDA for the *CLLC* converter. Gain model and ZVS range is usually analyzed by the approximation or numerical iterations [19]. Hence, fundamental harmonic approximation is applied in this article. The equivalent circuit is shown in Fig. 4 with the conditions of $L_a = {n_5}^2 L_c$ and $C_b = {n_5}^2 C_a$. The fundamental component of voltages and currents are given in

$$\begin{cases} v_{AB1} = \frac{4}{\pi} V_{bus1} \sin(\omega_s t - \varphi) \\ v_{CD1} = \frac{4}{\pi} V_{bus2} \sin(\omega_s t) \\ i_p = I_p \sin(\omega_s t - \varphi - \theta_1) \\ i_s = I_s \sin(\omega_s t + \theta_2) \end{cases}. \tag{3)–(6}$$

By Kirchhoff's law and energy conservation law, the normalized gain can be derived, as shown in (7), for the forward operation mode, where M_{gn} and Q, respectively, denote the normalized voltage gain and quality factor, as defined in (8) and (9). A detailed derivation process can be found in Appendix A, where the definitions of the resonant frequency f_r, the characteristic impedance R_0, the normalized frequency f_n, and the inductance ratio k ($= L_b/L_a$) are given

$$M_{gn} = \frac{\sin\varphi}{Q\left|\left(\frac{1}{f_n} - f_n\right)\left(2 + \frac{1}{k} - \frac{1}{k{f_n}^2}\right)\right|} \tag{7}$$

$$M_{gn} = \frac{n_5 V_{bus2}}{V_{bus1}} \tag{8}$$

$$Q = \frac{R_0}{8{n_5}^2 R_L/\pi^2}. \tag{9}$$

Because, the parameter and topology are symmetric, the gain model in backward mode is similar to the model in forward mode. The normalized gain in the backward mode is equal to $V_{bus1}/n_5 V_{bus2}$. The only difference is that the quality factor in backward mode changes when the transformer turn ratio n_5 is not equal to 1.

In the forward mode, the primary side switches can realize the ZVS turn-ON when i_p lags behind v_{AB}. Similarly, the secondary

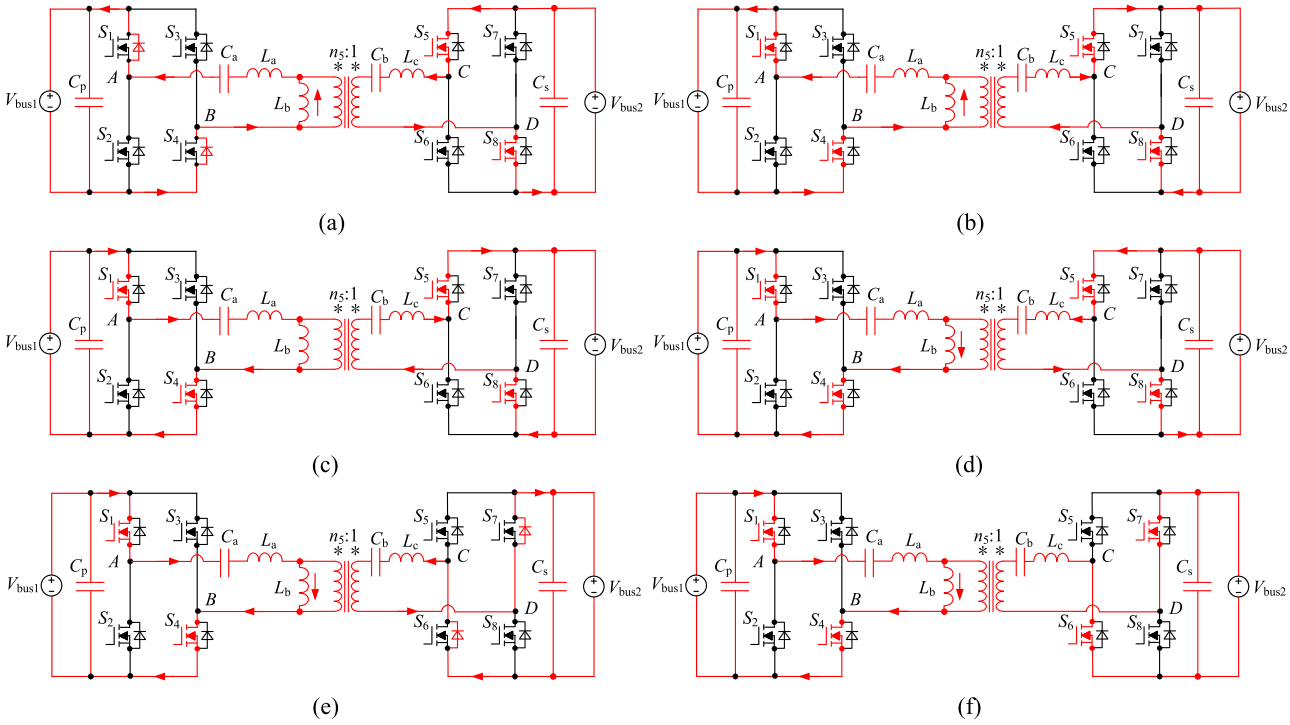

Fig. 3. Operation stages during half switching period. (a) Stage I: (t_0-t_1). (b) Stage II: (t_1-t_2). (c) Stage III: (t_2-t_3). (d) Stage IV: (t_3-t_4). (e) Stage V: (t_4-t_5). (f) Stage VI: (t_5-t_6).

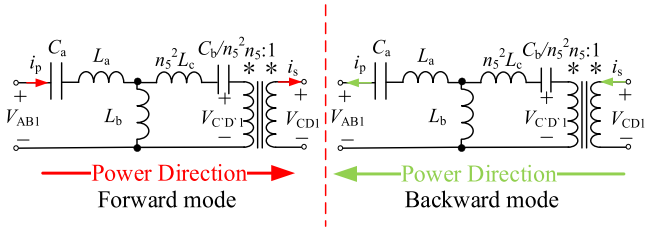

Fig. 4. Equivalent circuits in forward and backward modes.

side switches can realize the ZVS turn-ON when v_{CD} lags behind i_s. According to Appendix A, the ZVS conditions can be summarized in

$$\begin{cases} S_1\text{–}S_4 : \cos\varphi > \left(1+\frac{1}{k}-\frac{1}{kf_n{}^2}\right)\frac{1}{M_{gn}} \\ S_5\text{–}S_8 : \cos\varphi > \left(1+\frac{1}{k}-\frac{1}{kf_n{}^2}\right)M_{gn} \end{cases}. \quad (10)\text{–}(11)$$

In order to intuitively show the relationship between voltage gain and control variables, the three-dimensional (3-D) plot of M_{gn}-f_n-φ with different values of k is shown in Fig. 5 according to (7). It is clear that the gain plots show two infinitely large values for M_{gn}. In order to facilitate the analysis and the derivation process, the frequency values corresponding to these two infinitely large cases are defined as X_1 and X_2, respectively. Since Q is the coefficient in (7) and M_{gn} changes with the change of Q, Fig. 5 only shows the case that Q equals 1. From Fig. 5, it can be concluded that as follows.

1) The relationship between M_{gn} and f_n is *nonmonotonic*.
2) The frequency point X_1 gradually moves towards low frequency range when k increases. The frequency point X_2 is fixed.

III. Analysis about Gain and Soft-Switching Region

A. Analysis About the Gain Monotonicity With Respect to Phase Shift Angle

According to (7), the monotonicity of M_{gn} with respect to φ is related to the numerator of (7). In other words, M_{gn} shows a sinusoidal function with φ. A group of 2-D plots of M_{gn}-φ with different f_n is given in Fig. 6. Obviously, there are two monotonic intervals when φ changes from 0 to π. The monotonic increase interval is (0, π/2) and the monotonic decrease interval is (π/2, π). It is obvious that the harmonic will increase with the increase of the phase shift angle. Therefore, the variation range of φ is recommended to limited in (0, π/2).

B. Analysis About the Gain Monotonicity With Respect to Frequency

According to (7), the monotonicity of M_{gn} with respect to f_n is also related to its denominator, that is Y in (12). The monotonic interval depends on the zeros and extreme points of the function Y. A group of 2-D plots of M_{gn}- f_n with different φ is given in Fig. 7. X_1 and X_2 mentioned in Fig. 5 are given in (13) and (14), which are the solutions of f_n under the condition of $Y = 0$

$$Y = \left(\frac{1}{f_n}-f_n\right)\left(2+\frac{1}{k}-\frac{1}{kf_n{}^2}\right) \quad (12)$$

$$X_1 = \frac{1}{\sqrt{1+2k}} \quad (13)$$

$$X_2 = 1. \quad (14)$$

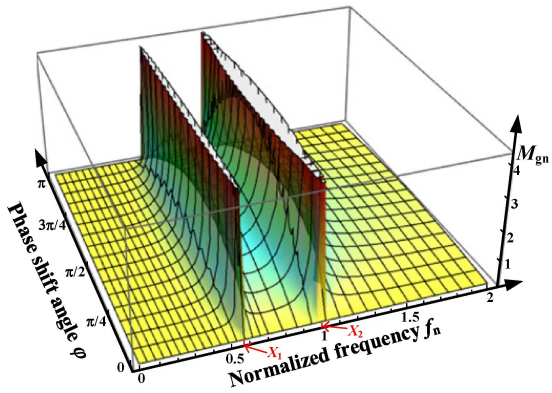

(a)

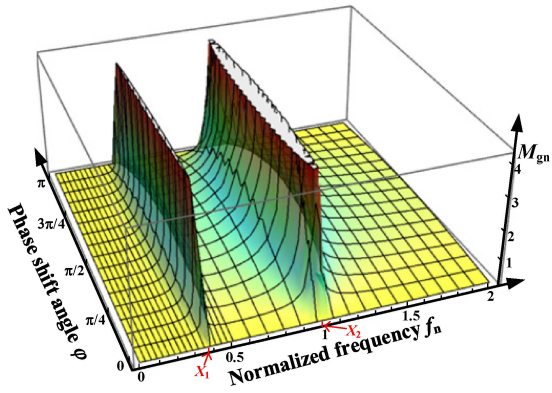

(b)

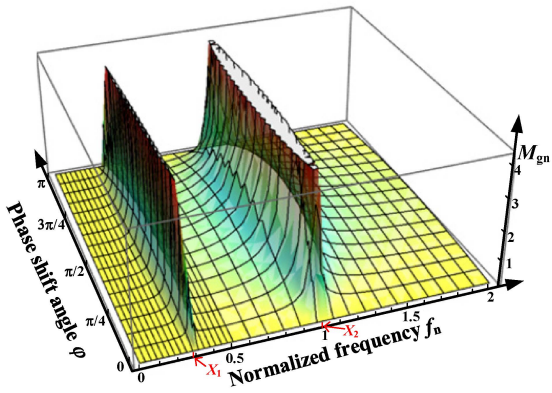

(c)

Fig. 5. Three-dimensional plots of M_{gn}-f_n-φ with $Q = 1$. (a) $k = 1$. (b) $k = 3$. (c) $k = 5$.

Y' and Y'' are defined, respectively, as the first-order and second-order derivatives of Y, as given in (15) and (16). If X is the zero point of Y' and meanwhile, Y'' is not equal to 0 at X, then, X is the extreme point of Y. Hence, the extreme point can be obtained as shown in (17), defined as X_3. The value of X_3 decreases with the increase of k according to (17)

$$Y' = \frac{2\left(\frac{1}{f_n} - f_n\right)}{k{f_n}^3} - \left(1 + \frac{1}{{f_n}^2}\right)\left(2 + \frac{1}{k} - \frac{1}{k{f_n}^2}\right) \quad (15)$$

$$Y'' = \frac{2\left(2 + \frac{1}{k} - \frac{1}{k{f_n}^2}\right)}{f_n^3} - \frac{6\left(\frac{1}{f_n} - f_n\right)}{k{f_n}^4} - \frac{4\left(1 + \frac{1}{{f_n}^2}\right)}{k{f_n}^3} \quad (16)$$

$$X_3 = \sqrt{\frac{\sqrt{k^2 + 8k + 4} - k - 1}{1 + 2k}}. \quad (17)$$

Obviously, $X_1 < X_3 < X_2 = 1$ is always satisfied. Hence, the monotonicity of M_{gn} with respect to f_n is obvious. The monotonic increase intervals are $(0, X_1)$ and $(X_3, 1)$, and meanwhile, the monotonic decrease intervals are (X_1, X_3) and $(1, +\infty)$. Designers often wish to find the monotonic relationship between the output and the control variable, so as to facilitate the design of the closed-loop control system. As mentioned above, there are four monotonic intervals in the frequency range. Normally, the switching frequency is always required to be set around 1 so as to decrease the harmonics. Hence, $(X_3, 1)$ and $(1, +\infty)$ are selected as the design region.

By (10) and (11), the 3-D plots of ZVS region with different values of M_{gn} are shown in Fig. 8. It is clear that most of the ZVS region is located within the range of $f_n < 1$. Obviously, the subinterval $(X_3, 1)$ is a better choice. The gain will be increased with the increase of switching frequency in the range of $(X_3, 1)$.

C. ZVS Region and Gain Contours With Respect to f_n and φ

According to (10) and (11), it is clear that S_5–S_8 are already in the soft-switching status if the ZVS condition for S_1–S_4 is satisfied when $M_{gn} < 1$. Similarly, when the converter is operated in a step-up mode, S_1–S_4 are already in soft switching statues when S_5–S_8 gradually enter their soft switching region. As a result, (10) and (11) can be simplified, as shown in (18) and (19). Similar conclusions can be found in the backward mode. The normalized voltage gain in the backward mode is equal to $V_{bus1}/n_5 V_{bus2}$.

The ZVS regions with different values of k and M_{gn} are shown in Fig. 9 with light blue color. The trend of ZVS region with increasing M_{gn} first broadens and then narrows when k is fixed. In other words, the ZVS region gradually narrows when M_{gn} increases or decreases from 1. Besides, the area of ZVS region decreases with the increase of k when M_{gn} is fixed, and meanwhile, the frequency range corresponding to the ZVS region gradually move towards the low frequency range. Therefore, when a wide gain variation range is required, k should be designed to be a smaller value

$$\begin{cases} \cos\varphi > \left(1 + \frac{1}{k} - \frac{1}{k{f_n}^2}\right)\frac{1}{M_{gn}}, & M_{gn} < 1 \\ \cos\varphi > \left(1 + \frac{1}{k} - \frac{1}{k{f_n}^2}\right) M_{gn}, & M_{gn} > 1 \end{cases}. \quad (18)\text{–}(19)$$

From (7), it can be seen that Q directly affect M_{gn}. The dashed line in Fig. 9 shows the contours of M_{gn} with different Q values. A ZVS turn-ON can be realized under a certain gain only when the desirable gain contours cross through the ZVS region in Fig. 9. It is clear that a ZVS turn-ON is easier to be realized when a smaller value is selected for Q.

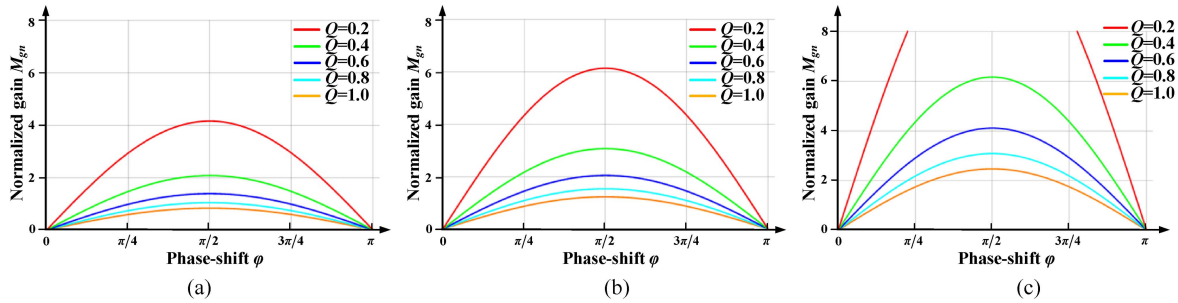

Fig. 6. Two-dimensional plots of M_{gn}-φ with different f_{n} in $k = 3$. (a) $f_{\mathrm{n}} = 0.7$. (b) $f_{\mathrm{n}} = 0.8$. (c) $f_{\mathrm{n}} = 0.9$.

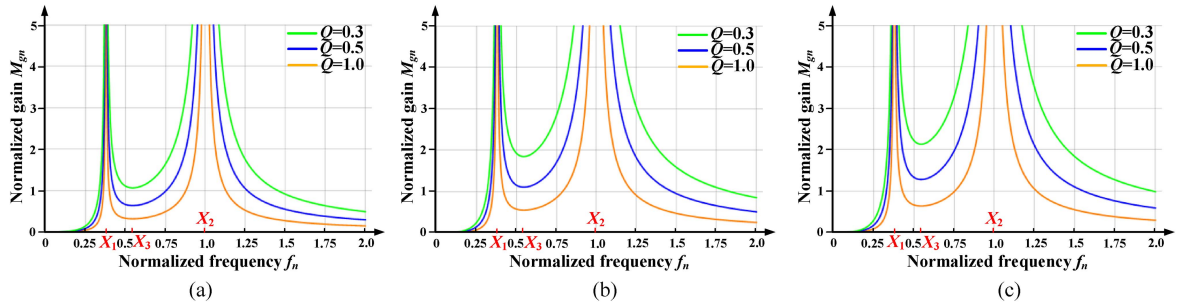

Fig. 7. Two-dimensional plots of M_{gn}-f_{n}. with different φ in $k = 3$. (a) $\varphi = \pi/6$. (b) $\varphi = \pi/3$. (c) $\varphi = \pi/2$.

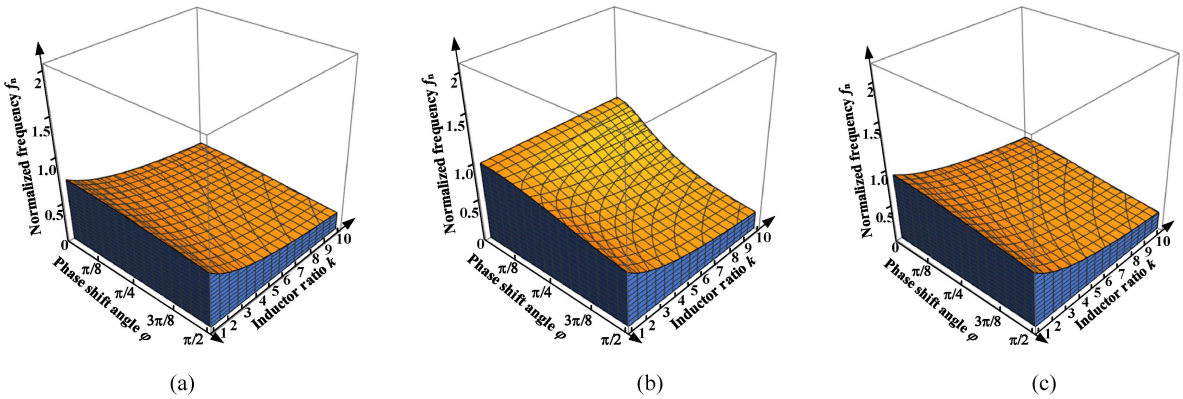

Fig. 8. Three-dimensional plots of ZVS region with respect to f_{n}, φ, and k under different gains. (a) $M_{\mathrm{gn}} = 0.5$. (b) $M_{\mathrm{gn}} = 1.0$. (c) $M_{\mathrm{gn}} = 1.5$.

Since Q is related to the load resistance R_{L}, the soft-switching realization in a wide load range means that the gain contour clusters of the desired Q values should cross the ZVS region in Fig. 9. As mentioned before, the smaller the Q, the easier it is to implement ZVS. Therefore, when the design process of circuit parameter is carried out, the maximum value of Q should be focused on. Normally, $Q_{\max} = 0.5 \sim 0.6$ is suggested.

IV. Circuit Parameter Design Method

The design steps are summarized to a flowchart, as shown in Fig. 10.

Step 1. Determination for the transformer turns ratio n_5: For the bidirectional converters, the complexity of parameter design process will be increased if the voltage ranges of the two ports are different. Therefore, a design method of symmetric voltage range and symmetric parameters is proposed, so that the converter can also cover the reverse operating condition with the forward parameter design.

For the parameter design process, it is easiest when both ends of the resonant tank are with the same voltage range. Hence, the transformer turns ratio n_5 can be determined first to realize a symmetrical voltage range for the resonant tank.

It is assumed that the input voltage range of the converter is $V_{\mathrm{bus1min}} \sim V_{\mathrm{bus1max}}$ and the output voltage range is $V_{\mathrm{bus2min}} \sim V_{\mathrm{bus2max}}$, where these two ranges may differ greatly. Fig. 11 lists all the situations between these two voltage ranges: included (e, k), overlapped (a, c, g, i), and disjoint (b, d, h, j). However, all these situations can be simplified into two cases (f and l) for the resonant tank with a proper transformer

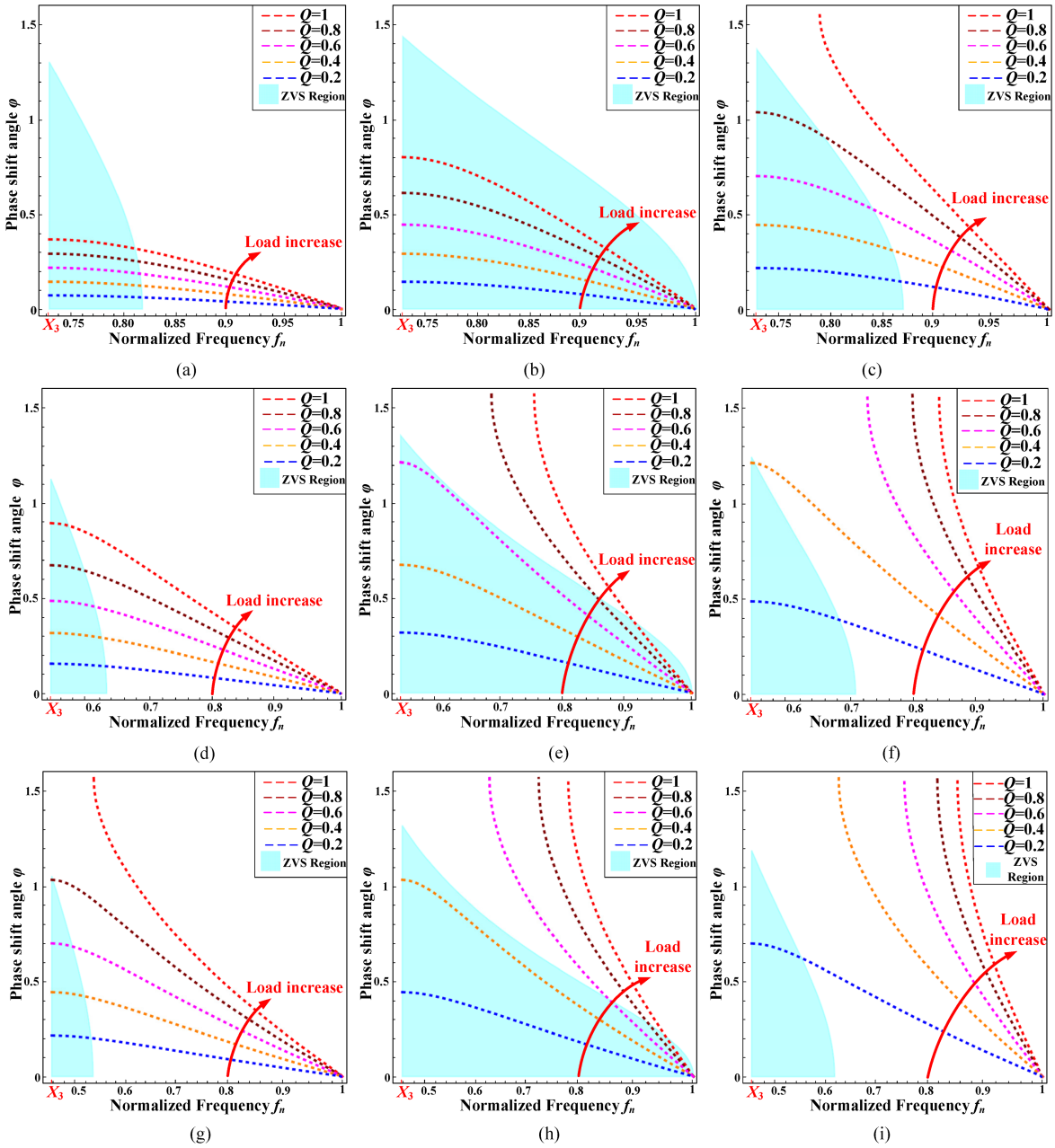

Fig. 9. ZVS region and the gain contour clusters with different k and $M_{\rm gn}$. (a) $k=1$, $M_{\rm gn}=0.5$. (b) $k=1$, $M_{\rm gn}=1$. (c) $k=1$, $M_{\rm gn}=1.5$. (d) $k=3$, $M_{\rm gn}=0.5$. (e) $k=3$, $M_{\rm gn}=1$. (f) $k=3$, $M_{\rm gn}=1.5$. (g) $k=5$, $M_{\rm gn}=0.5$. (h) $k=5$, $M_{\rm gn}=1$. (i) $k=5$, $M_{\rm gn}=1.5$.

turns ratio. By setting the transformer turns ratio n_5 equal to $V_{\rm bus1min}/V_{\rm bus2min}$, both ends of the resonant tank face the similar voltage variation range. Then, the normalized maximum and minimum of voltage for the resonant tank are $V_{\max}=\max\{V_{\rm bus1max},\ n_5V_{\rm bus2max}\}$ and $V_{\min}=\min\{V_{\rm bus1min},\ n_5V_{\rm bus2min}\}$, respectively. As result, the transformer turns ratio n_5 can be designed according to

$$n_5=\frac{V_{\rm bus1\,min}}{V_{\rm bus2\,min}}. \tag{20}$$

Step 2. Calculation for the normalized voltage gain range: The normalized voltage gain range can be calculated according to

$$M_{\rm gn-max}=\frac{\max\{V_{\rm bus1\,max},n_5V_{\rm bus2\,max}\}}{V_{\rm bus1\,min}} \tag{21}$$

$$M_{\rm gn-min}=\frac{n_5V_{\rm bus2\,min}}{\max\{V_{\rm bus1\,max},n_5V_{\rm bus2\,max}\}}. \tag{22}$$

Step 3. Selection for an inductance ratio k: As mentioned in Section III-C, it is clearly seen that a wide ZVS region can be obtain with a small k. However, a small value for k normally results in a small magnetizing inductance and a high rms value of the circulating current. Therefore, the choice of k needs to

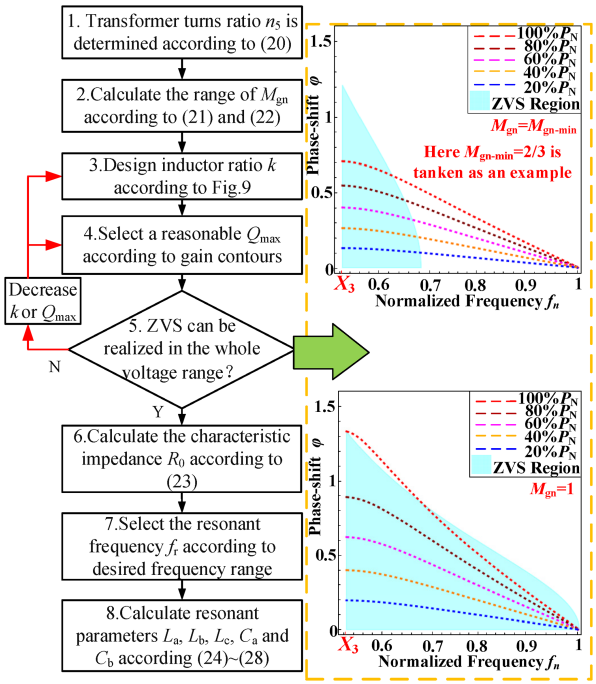

Fig. 10. Flowchart of the parameter design process.

take both the soft switching realization and the efficiency into account. Normally, k values in the range of 3–5 are recommended as initial conditions for design, which is similar as the selection of inductor ratio in a unidirectional *LLC* converter [10].

Step 4. Selection for the maximum quality factor Q_{max}: As mentioned in Section III-C, when Q gets smaller, the gain contour plots are more likely to intersect the ZVS region. Therefore, we need to be concerned about whether the gain contour intersects the ZVS region for different gains when the quality factor reaches its maximum value $Q_{\max}$. This value in the range of 0.5~0.6 are recommended as initial conditions for design.

Step 5. Check the ZVS realization in the whole voltage range: After k is selected, it is suggested to plot the gain contour clusters with different Q values and the ZVS region by a mathematic software, similar as Fig. 9, so as to check whether the soft-switching can be realized at the gain boundary and load boundary. It is necessary to focus on the intersection of the gain contours and the soft-switch region at $M_{\rm gn}=1$ and $M_{\rm gn}=M_{\rm gn\text{-}min}$, which are corresponding to the cases that $n_5\times V_{\rm bus2}$ equals $V_{\min}$ and meanwhile the input voltage $V_{\rm bus1}$, respectively, equals $V_{\min}$ and $V_{\max}$. If not, k or $Q_{\max}$ can be decreased to a smaller value.

The reason that we need to check the cases of $M_{\rm gn}=1$ and $M_{\rm gn}=M_{\rm gn\text{-}min}$ can be explained as follows: quality factor Q reaches the maximum value when $n_5\times V_{\rm bus2}$ decreases to its minimum value $V_{\min}$ at rated power. Since the gain contours are plotted by (7) and the soft-switching region is plotted by (18) and (19), which are all affected by the gain, so the minimum and maximum input voltages should also be taken into account.

Step 6. Calculation for the characteristic impedance R_0: R_0 is calculated by (23) after the k and $Q_{\max}$ are determined

$$R_0=Q_{\max}\frac{8n_5^2}{\pi^2}\frac{V_{\rm bus2\,min}{}^2}{P_{\rm N}}. \tag{23}$$

Step 7. Selection for the resonant frequency f_r: The resonant frequency $f_{\rm r}$ is selected according to the desired switching frequency range so to reduce the harmonics.

Step 8. Calculation for the resonant tank parameters: With the mentioned design results, the resonant tank parameters can be calculated according to

$$\begin{cases} L_{\rm a}=R_0/2\pi f_{\rm r} \\ L_b=kL_a \\ L_c=L_{\rm a}/n_5^2 \\ C_a=1/(R_0 2\pi f_{\rm r}) \\ C_b=n_5^2C_a \end{cases}. \tag{24)–(28}$$

V. Proposed Control Strategy

A. Proposed Linear Function Between f_n and φ

The ZVS region is fixed after the circuit parameters have been determined. Therefore, a relationship between these two control variables, which are the phase shift angle and the switching frequency, will be proposed in this section in order to ensure the soft-switching realization during the whole voltage variation range and load range. Since the linear function ($\varphi=\mathrm{K_m}\times f_{\rm n}+\mathrm{B_m}$) is the simplest function to describe the relationship between two variables, it is utilized to make a relationship between $f_{\rm n}$ and φ.

Fig. 12 is an example to show how to select a proper linear function. The contour plots are with the same voltage gain ($M_{\rm gn}=1.5$) but with different quality factors, as well as the load resistance. As mentioned in Section III-C, the necessary condition for the soft-switching realization is that the contour plots must intersect with the ZVS region. Three possible linear functions (Track 1–Track 3) are given in Fig. 12 to make a comparison. The converter may lose the soft-switching under heavy load condition if the third track is selected. Although the first track can cover a wide soft-switching range, it also results in a wide frequency range, which is not facilitate to the transformer design. Therefore, the determination for the linear function must make a trade of the soft-switching range and the frequency range. In Fig. 12, the second track reserves the advantages for both the narrow frequency range and the wide ZVS realization for the load variation. Moreover, since Track 2 is close to the boundary of the ZVS region, the turn-OFF current value of the power switches is small, which is conducive to reducing the backflow power and improving the efficiency.

According to Section III-C, the ZVS region changes with different voltage gains. Therefore, the linear function should be adjusted under different voltage gains ($M_{\rm gn}$) in order to realize a wide soft-switching range. Therefore, $\varphi=\mathrm{K_m}\times f_{\rm n}+\mathrm{B_m}$ represents the linear function with tunable slope ($\mathrm{K_m}$) and intercept ($\mathrm{B_m}$) under different gains. According to the trend of the ZVS region under different gains in Fig. 9, the linear functions $\varphi=\mathrm{K_m}\times f_{\rm n}+\mathrm{B_m}$ should be designed with the consideration of both the widest and narrowest soft switching range. Then, the slopes ($\mathrm{K_m}$) and intercepts ($\mathrm{B_m}$) at other gains can be fitted with a function with respect to $M_{\rm gn}$.

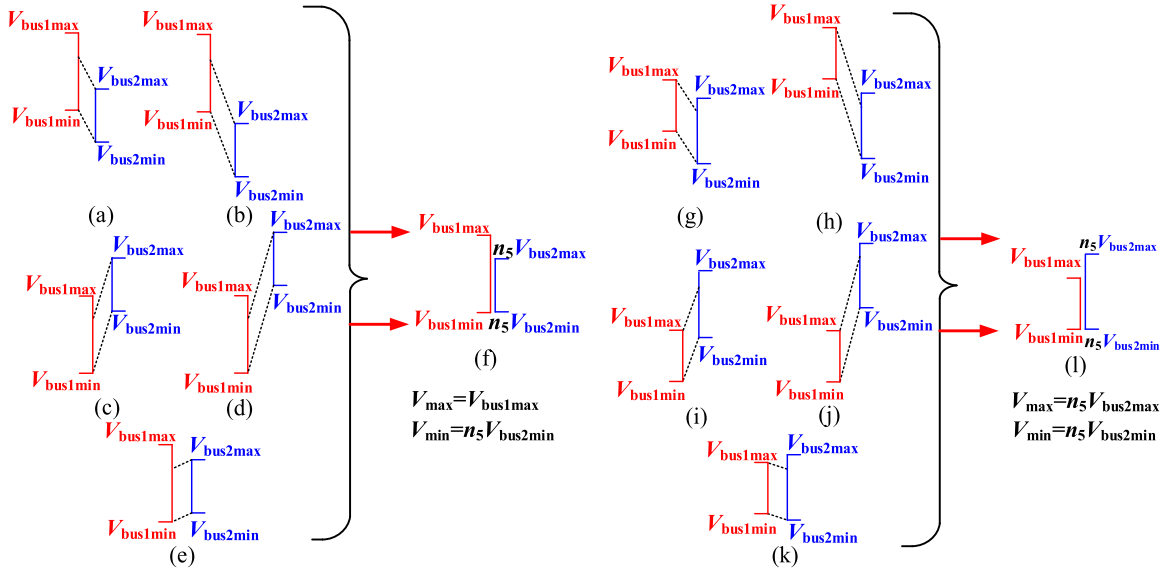

Fig. 11. Schematic diagram of two port voltages after simplification by employing the transformer turns ratio n_5.

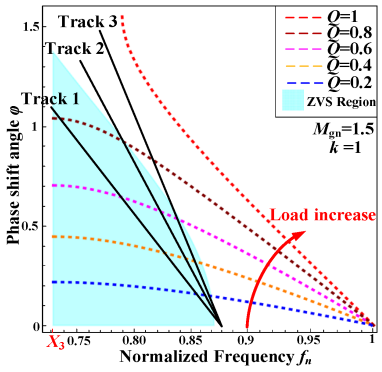

Fig. 12. Three operating tracks for f_n and φ. ($M_{gn} = 1.5, k = 1$).

TABLE I
SYMBOLS OF THE SLOPES AND INTERCEPTS OF THE PROPOSED LINEAR FUNCTION ($\varphi = K_M \times F_N + B_M$) CORRESPONDING TO FIG. 13

Gain value	$M_{gn\text{-}min}=1/M_{gn\text{-}max}$	1	$M_{gn\text{-}max}$
slope	K_2	K_1	K_2
intercept	B_2	B_1	B_2

The variation range of M_{gn} can be calculated after n_5 is established by (20). The ZVS region area is minimal if M_{gn} is equal to $M_{gn\text{-}min}$ or $M_{gn\text{-}max}$. Here, the specification of our prototype is taken as the example to generate Fig. 13 so as to intuitively explain how to design the control strategy. The specification requires a bidirectional converter with 1 kW rated power and both ports should cover the range of 80 V–120 V.

By our proposed design method for the circuit parameters, M_{gn_min} is the reciprocal of M_{gn_max}. The symbols of the slopes and intercepts for the cases of $M_{gn} = M_{gn\text{-}min}(= 1/M_{gn\text{-}max})$, $M_{gn} = 1$, and $M_{gn} = M_{gn\text{-}max}$, are defined in Table I, respectively. It should be noted that two reciprocal gain values correspond to the same soft switching region according to (18) and (19). Hence, the soft-switching regions of $M_{gn} = M_{gn\text{-}min}$ and $M_{gn} = M_{gn\text{-}max}$ are with the same shape. Besides, the gain contours with the same power under two reciprocal gains can be totally the same according to (7)–(9), such as the dash lines in Fig. 13(a) and (c). Therefore, if two gains exhibit a reciprocal relationship, the converter can be operated with the same linear function, such as the operating track in Fig. 13(a) and (c). This is why we use the same symbols to denote the slope (or intercept) in the conditions of $M_{gn\text{-}min}$ and $M_{gn\text{-}max}$.

The ZVS region area is largest when M_{gn} is equal to 1, so the slope can be selected with a higher value to reduce the switching frequency range within the load range, such as the operating track in Fig. 13(b). After determining the numerical values of K_1, B_1, K_2, and B_2 in the soft-switching region, the dummy variables (K_m, B_m) of the proposed linear function (29) can be calculated online by a MCU corresponding to different voltage gains based on (30) and (31) in Table II. It is suggested that the soft-switching realization for other operation conditions is also checked with the preset linear function. If the operating track is outside the soft-switching region, K_1 and B_1 can be adjusted. By this means, the frequency range can be limited into

TABLE II
PARAMETER ADJUSTMENT METHOD FOR K_M AND B_M IN THE PROPOSED LINEAR FUNCTION ($\varphi = K_M \times F_N + B_M$)

Symbol	*Function Expressions*	
φ	$\varphi = K_m f_n + B_m$	(29)
K_m	$\begin{cases} \frac{K_2-K_1}{M_{gn\text{-}max}-1}\frac{1}{M_{gn}}+\frac{K_1M_{gn\text{-}max}-K_2}{M_{gn\text{-}max}-1}, & M_{gn}\le 1 \\ \frac{K_2-K_1}{M_{gn\text{-}max}-1}M_{gn}+\frac{K_1M_{gn\text{-}max}-K_2}{M_{gn\text{-}max}-1}, & M_{gn}>1 \end{cases}$	(30)
B_m	$\begin{cases} \frac{B_2-B_1}{M_{gn\text{-}max}-1}\frac{1}{M_{gn}}+\frac{B_1M_{gn\text{-}max}-B_2}{M_{gn\text{-}max}-1}, & M_{gn}\le 1 \\ \frac{B_2-B_1}{M_{gn\text{-}max}-1}M_{gn}+\frac{B_1M_{gn\text{-}max}-B_2}{M_{gn\text{-}max}-1}, & M_{gn}>1 \end{cases}$	(31)

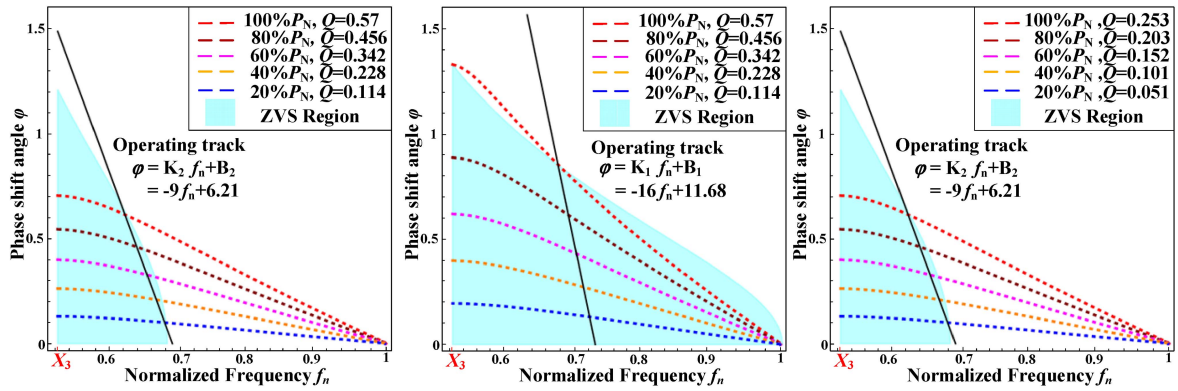

Fig. 13. Operating tracks considering boundaries with different voltage gains. (a) $M_{gn} = 2/3$ ($V_{in} = 120$ V, $V_{out} = 80$ V). (b) $M_{gn} = 1$ ($V_{in} = 80$ V, $V_{out} = 80$ V). (c) $M_{gn} = 1.5$ ($V_{in} = 80$ V, $V_{out} = 120$ V).

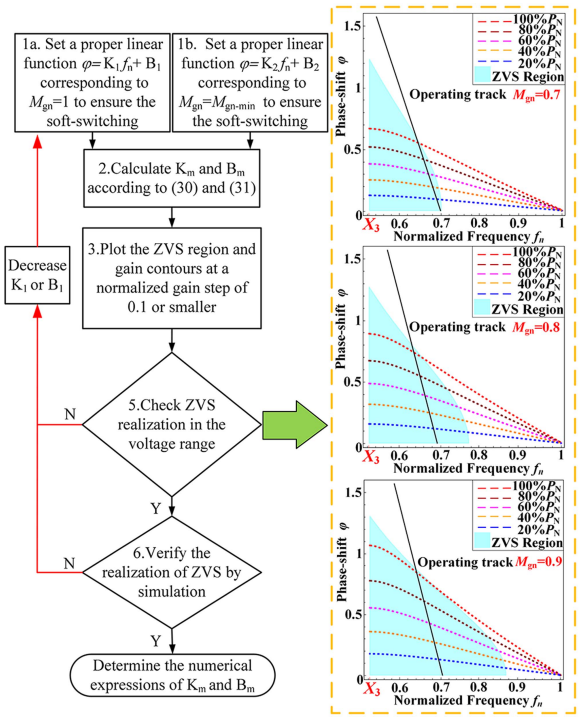

Fig. 14. Flowchart of adjustable control parameter design process.

a small value range but achieve a wide voltage range and load range. A flow chart of design process for the adjustable linear function $\varphi = K_m \times f_n + B_m$ is summarized in Fig. 14.

B. Feedforward Control Algorithm

In order to accelerate the step response of the converter, a feedforward control algorithm is proposed.

By substituting the linear function $\varphi = K_m \times f_n + B_m$ into (7) and expanding $M_{gn} \times Q$ according to the definition, (32) can be obtained. Although f_n can be calculated according to (32) theoretically if the output voltage and current are detected, the analytical solution for f_n is very complicated and impractical for

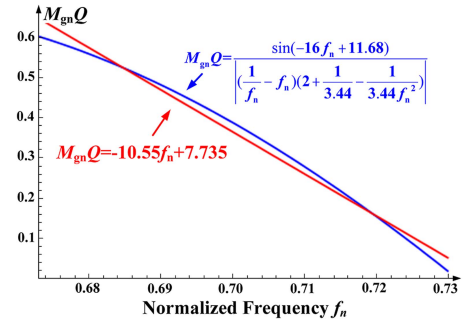

Fig. 15. Example of the curve fitting method for the feedforward controller realization ($K_m = -16$, $B_m = 11.68$, $M_{gn} = 1$).

the realization of the control system. Here, a curve fitting method is applied to get an approximation expression of f_n. Fig. 15 shows the example as follows.

1) $M_{gn} \times Q$ can be treated as a whole object and it can be easily plotted with respect to f_n according to (32), such as the blue curve in Fig. 15.
2) Setting a straight line across the blue curve and using a linear function to solve the analytical solution of f_n, such as the red line in Fig. 15. By this method, the solution of f_n is the approximation value of the feedforward controller. The effectiveness of this feedforward controller is examined in Section VI-D with the same PI parameters

$$M_{gn}Q = \frac{\sin(K_m \times f_n + B_m)}{\left|\left(\frac{1}{f_n} - f_n\right)\left(2 + \frac{1}{k} - \frac{1}{k f_n^2}\right)\right|} = \frac{\pi^2 R_0 I_{bus2}}{8 n_5 V_{bus1}}. \quad (32)$$

The control block diagram in forward mode is given, as shown in Fig. 16. Due to the symmetric circuit parameters, the control strategy in backward mode is the same as the forward mode. The steady-state waveforms and dynamic response are provided in Section VI.

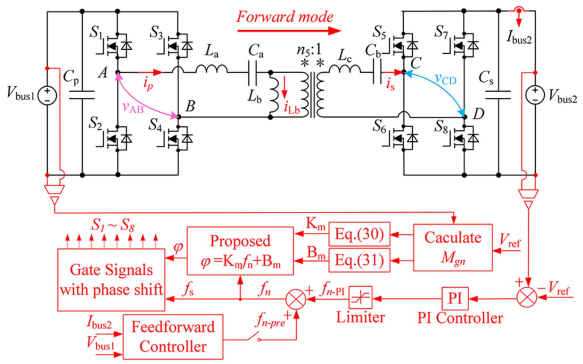

Fig. 16. Block diagram of the closed-loop control system in forward mode.

TABLE III
MAIN CIRCUIT PARAMETERS OF THE CLLC PROTOTYPE AND SPECIFICATION

Parameters	Value
Primary bus voltage V_{bus1}	80 V–120 V
Secondary bus voltage V_{bus2}	80 V–120 V
Nominal output power P_N	1 kW
Transformer Turns ratio n_5 (N_p:N_s)	1:1
Primary resonant capacitor C_a	430 nF
Primary resonant inductor L_a	3.77 μH
Magnetizing inductor L_b	12.97 μH
Primary resonant inductor L_c	3.77 μH
Secondary resonant capacitor C_b	430 nF

VI. EXPERIMENTAL RESULT AND COMPARISON

In order to verify the effectiveness of the proposed control strategy and parameter design method, a 1 kW prototype is built and tested. The main circuit parameters of the *CLLC* resonant converter can be calculated according to the proposed design method, which are given in Table III. The linear function corresponding to the soft-switching boundaries can be obtained according to Section V-A. The results of slope and intercept are $K_m = 14 \times M_{gn} - 30$ and $B_m = -10.94 \times M_{gn} + 22.62$ if $M_{gn} > 1$ while $K_m = 14/M_{gn} - 30$ and $B_m = -10.94/M_{gn} + 22.62$ if $M_{gn} \leq 1$.

A. CLLC and LLC-C Parameter Equivalence

Zahid et al. [20] and Tan and Ruan [21] indicated the *CLLC* resonant converter [see Fig. 1(b)] is fully equivalent to *LLC-C* resonant converter [see Fig. 1(c)]. Since *LLC-C* resonant converter is with a smaller number of components, the prototype is finally realized by a *LLC-C* resonant converter. The main circuit parameters of the *LLC-C* converter are given in Table IV, where the resonant parameters are calculated by Appendix B. The prototype photo is shown in Fig. 17.

B. Forward Mode Test

The steady state waveforms under 1 kW condition are given in Figs. 18 and 19, where the ZVS realizations of four boundary operating points are shown. Besides, light load conditions

TABLE IV
MAIN CIRCUIT PARAMETERS IN THE PROTOTYPE OF THE LLC-C CONVERTER

Parameters	Value
Primary bus voltage V_{bus1}	80 V–120 V
Secondary bus voltage V_{bus2}	80 V–120 V
Nominal output power P_N	1 kW
Transformer Turns ratio n_4 (N_p:N_s)	7:9
Primary resonant capacitor C_{r1}	423 nF (47nF/630V x9)
Primary resonant inductor L_r	6.7 μH (3C95-PQ50)
Magnetizing inductor L_m	10 μH (DMR95-PQ50)
Secondary resonant capacitor C_{r2}	423 nF (47nF/630V x9)
Switches S_1–S_8	FDH055N15A x2

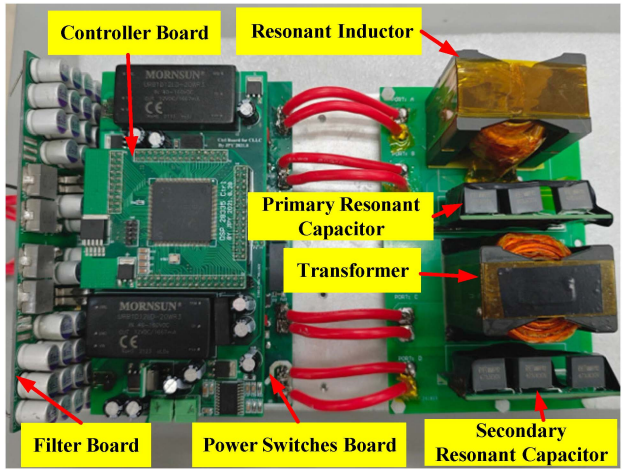

Fig. 17. Prototype photo.

(200 W, 20% nominal load) are also tested to verify the feasibility of the control strategy. The ZVS realizations under 20% nominal load condition are given in Figs. 20 and 21. The efficiency performance in the forward mode is given in Fig. 22, and the full-load efficiency is in the range of 96.19%–98.10%. The variation range of switching frequency is from 76.35 kHz to 90.67 kHz in the whole voltage and load range.

C. Backward Mode Test

The steady-state waveforms in backward mode are given in Figs. 23, 24, 25, and 26. The efficiency performance is provided in Fig. 27. Due to the design method of symmetric circuit parameters, the key waveforms in backward mode are with the similar performance as the forward mode. Besides, the efficiency performance is also similar as forward mode, where the rated-power efficiency is in the range of 96.22%–98.24%. The variation range of switching frequency is from 76.41 to 90.73 kHz in whole voltage and load range.

D. Dynamic Test

In order to prove the continuity of the proposed control strategy, a 50% load step response is tested. Moreover, the feedforward control algorithm is also applied, as shown in Figs. 28, 29,

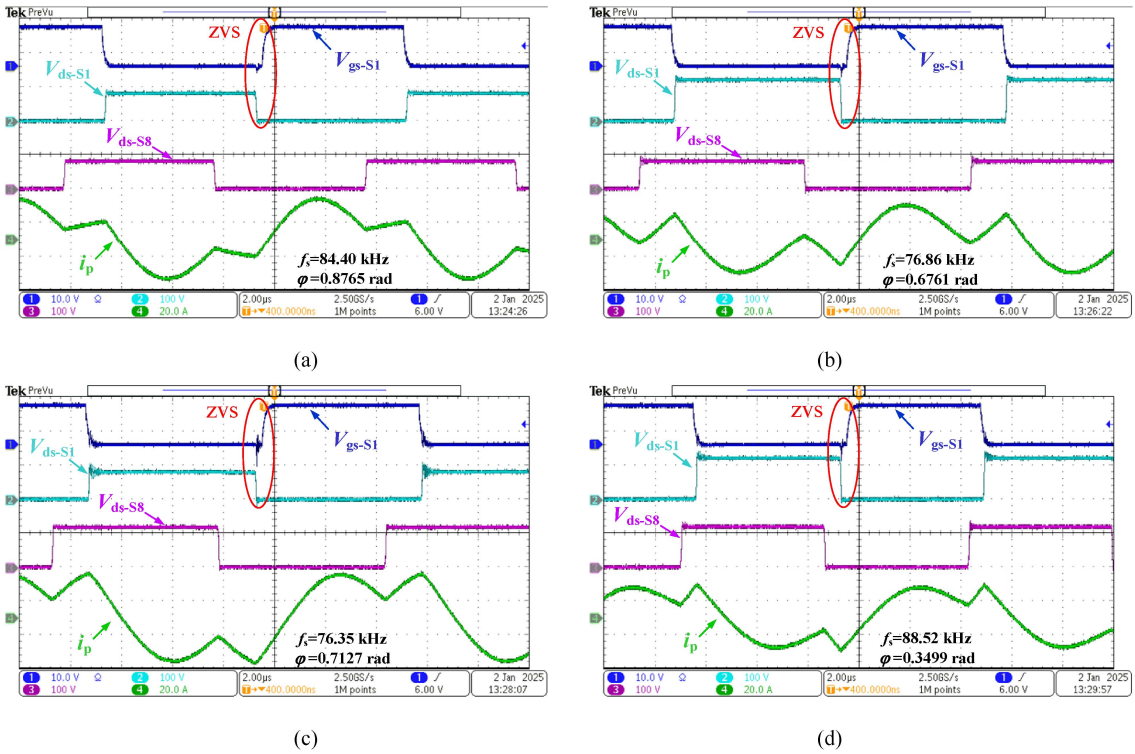

Fig. 18. ZVS realization of the primary side switches at full load in the forward mode. (a) $V_{\mathrm{bus1}} = 80$ V, $V_{\mathrm{bus2}} = 80$ V. (b) $V_{\mathrm{bus1}} = 120$ V, $V_{\mathrm{bus2}} = 80$ V. (c) $V_{\mathrm{bus1}} = 80$ V, $V_{\mathrm{bus2}} = 120$ V. (d) $V_{\mathrm{bus1}} = 120$ V, $V_{\mathrm{bus2}} = 120$ V.

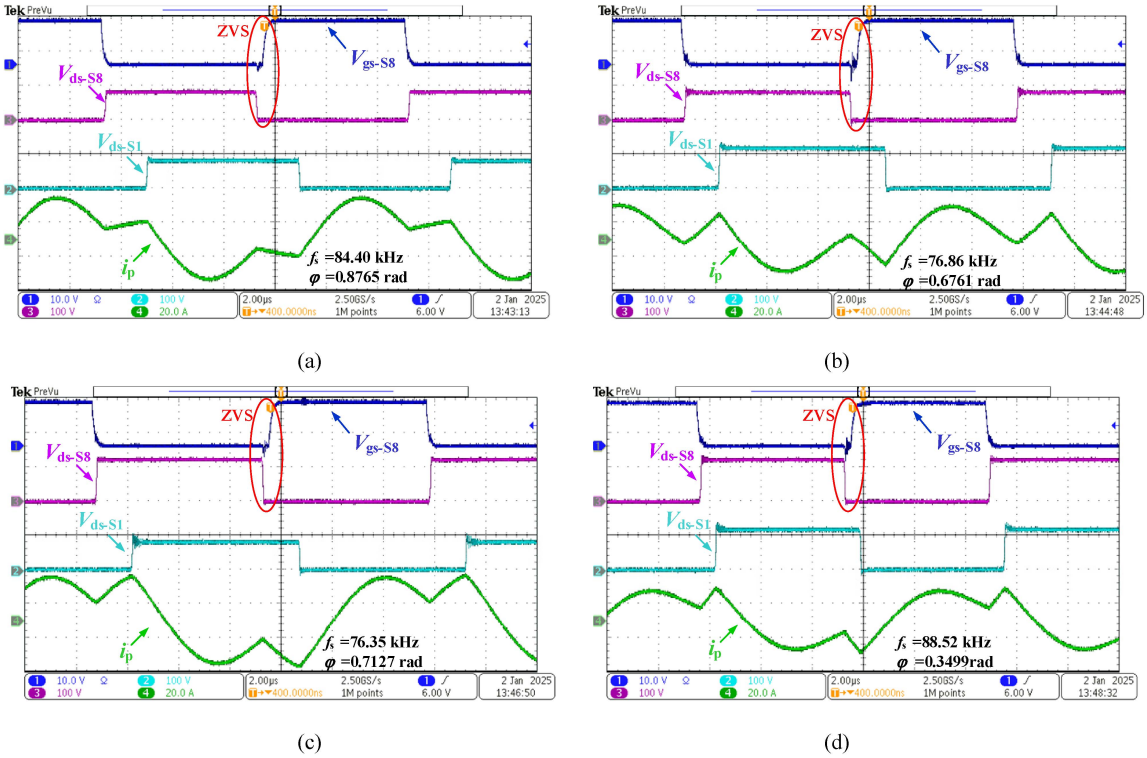

Fig. 19. ZVS realization of the secondary side switches at full load in the forward mode. (a) $V_{\mathrm{bus1}} = 80$ V, $V_{\mathrm{bus2}} = 80$ V. (b) $V_{\mathrm{bus1}} = 120$ V, $V_{\mathrm{bus2}} = 80$ V. (c) $V_{\mathrm{bus1}} = 80$ V, $V_{\mathrm{bus2}} = 120$ V. (d) $V_{\mathrm{bus1}} = 120$ V, $V_{\mathrm{bus2}} = 120$ V.

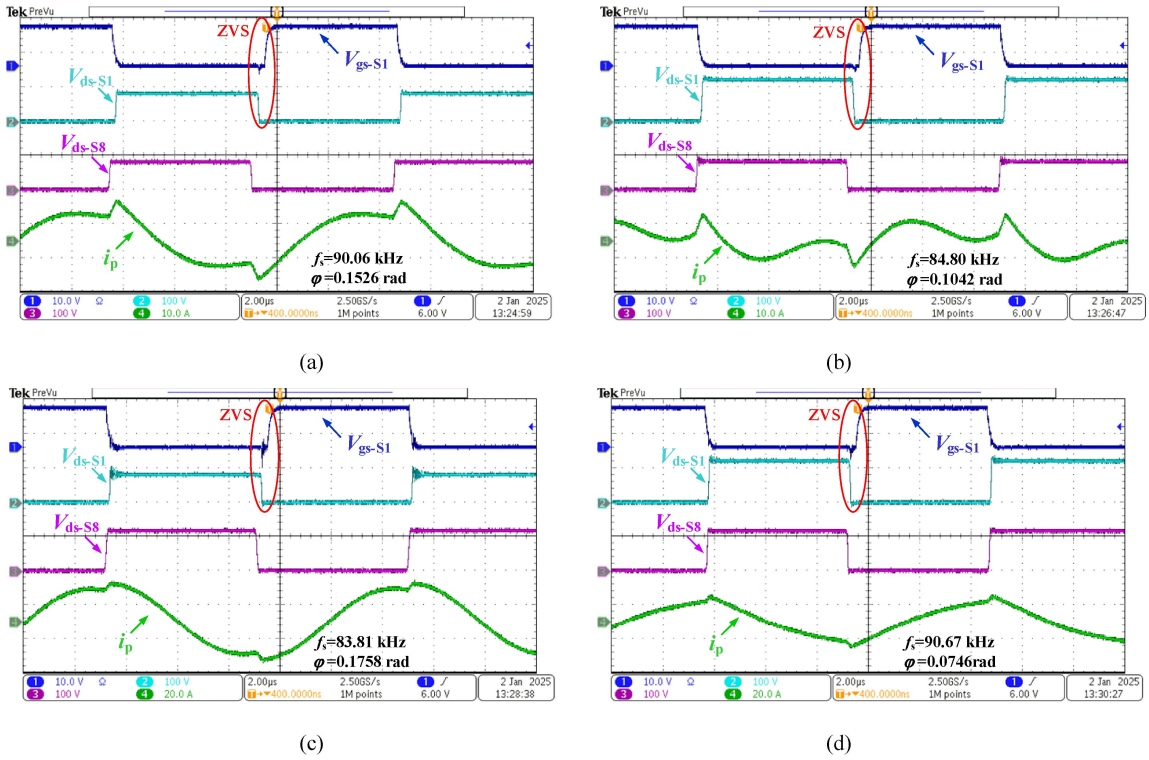

Fig. 20. ZVS realization of the primary side switches at 20% nominal load in the forward mode. (a) $V_{\mathrm{bus1}} = 80$ V, $V_{\mathrm{bus2}} = 80$ V. (b) $V_{\mathrm{bus1}} = 120$ V, $V_{\mathrm{bus2}} = 80$ V. (c) $V_{\mathrm{bus1}} = 80$ V, $V_{\mathrm{bus2}} = 120$ V. (d) $V_{\mathrm{bus1}} = 120$ V, $V_{\mathrm{bus2}} = 120$ V.

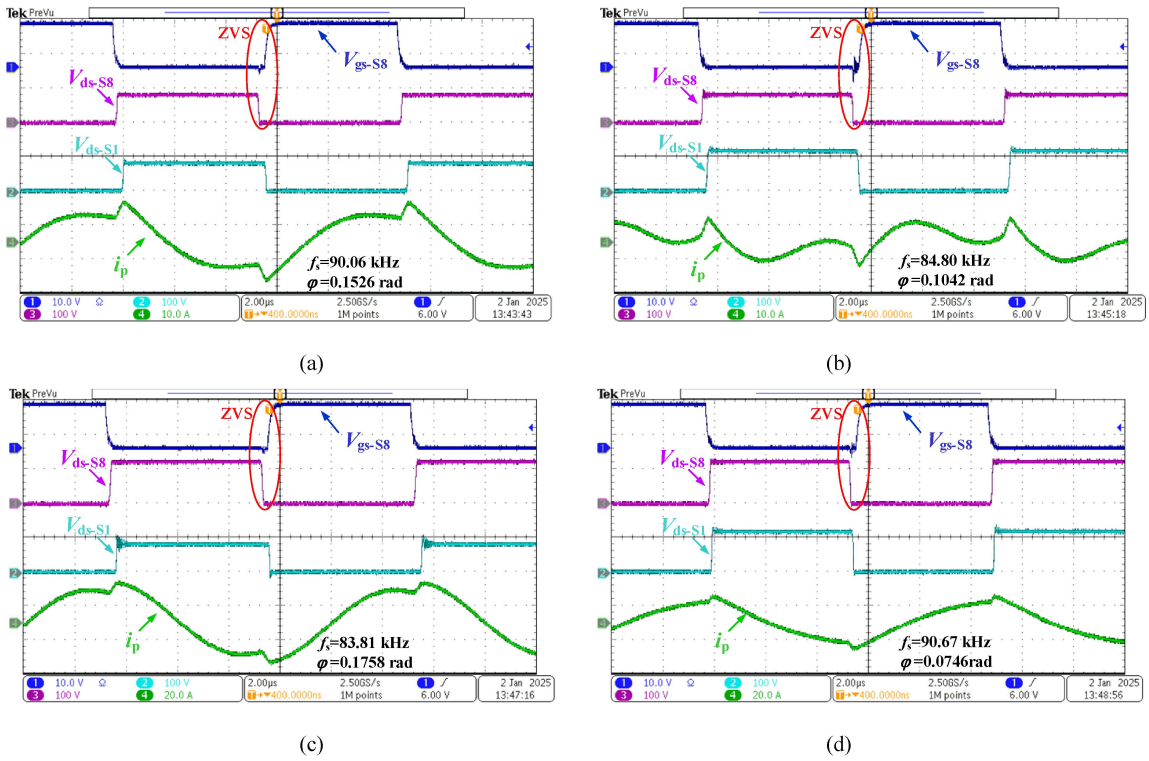

Fig. 21. ZVS realization of the secondary side switches at 20% nominal load in the forward mode. (a) $V_{\mathrm{bus1}} = 80$ V, $V_{\mathrm{bus2}} = 80$ V. (b) $V_{\mathrm{bus1}} = 120$ V, $V_{\mathrm{bus2}} = 80$ V. (c) $V_{\mathrm{bus1}} = 80$ V, $V_{\mathrm{bus2}} = 120$ V. (d) $V_{\mathrm{bus1}} = 120$ V, $V_{\mathrm{bus2}} = 120$ V.

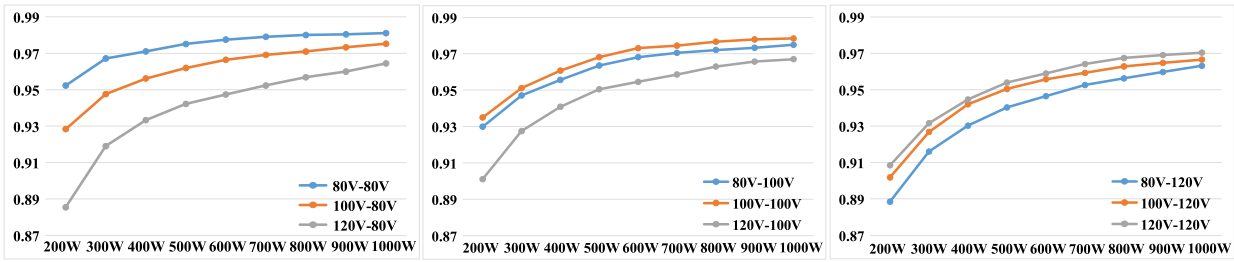

(a) (b) (c)

Fig. 22. Efficiency performance of the prototype in forward mode. (a) $V_{\mathrm{bus1}} = 80$ V–120 V, $V_{\mathrm{bus2}} = 80$ V. (b) $V_{\mathrm{bus1}} = 80$ V–120 V, $V_{\mathrm{bus2}} = 100$ V. (c) $V_{\mathrm{bus1}} = 80$ V$\sim$120 V, $V_{\mathrm{bus2}} = 120$ V.

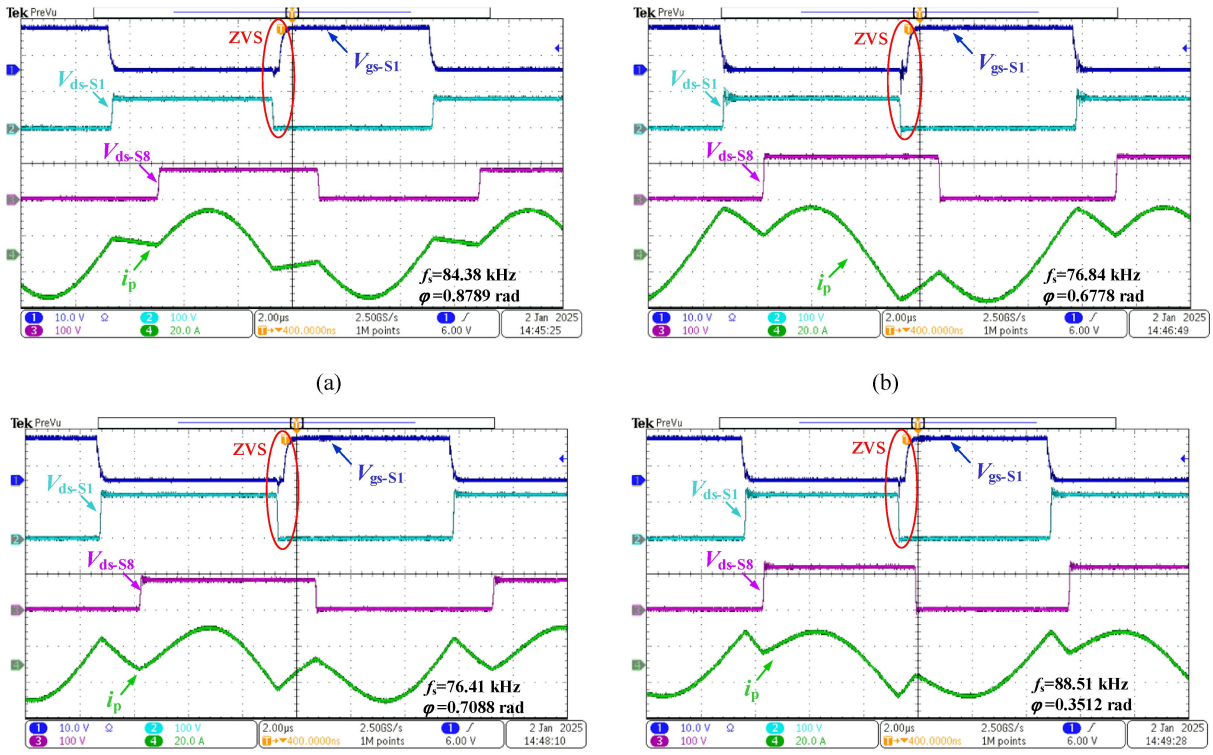

(a) (b) (c) (d)

Fig. 23. ZVS realization of the primary side switches at full load in the backward mode. (a) $V_{\mathrm{bus2}} = 80$ V, $V_{\mathrm{bus1}} = 80$ V. (b) $V_{\mathrm{bus2}} = 120$ V, $V_{\mathrm{bus1}} = 80$ V. (c) $V_{\mathrm{bus2}} = 80$ V, $V_{\mathrm{bus1}} = 120$ V. (d) $V_{\mathrm{bus2}} = 120$ V, $V_{\mathrm{bus1}} = 120$ V.

30, and 31. It is proved that the load step response is significantly improved after the feedforward controller is enabled.

E Comparison

The purpose of our proposed method is to make a good balance between the frequency range, efficiency, reliability (elimination of core saturation), and bidirectional voltage range for the practical realization for engineering. As explained in Fig. 1, *LLC-L, CLLC,* and *LLC-C* resonant tank can be all considered derived from the *LLC* traditional resonant tank, therefore, some state-of-the-arts with these resonant tanks are given in Table V to make a comparison with the proposed method from the following aspects.

1) Core Saturation Risk (Reliability of the Converter): The reason that *CLLC* (*LLC-C*) converter is selected as our topology is due to the existence of the primary-side and secondary-side capacitors, which can naturally eliminate the core saturation risk. In Table V, Jiang et al. [29], Jia et al. [32], and Wu et al. [34] may face this risk due to the lack of the blocking capacitors. Take the *LLC-L* tank in Fig. 1(a) for an example, the auxiliary inductor L_{m1} may be saturated in forward mode while the transformer may be saturated in backward mode, especially in high power applications.

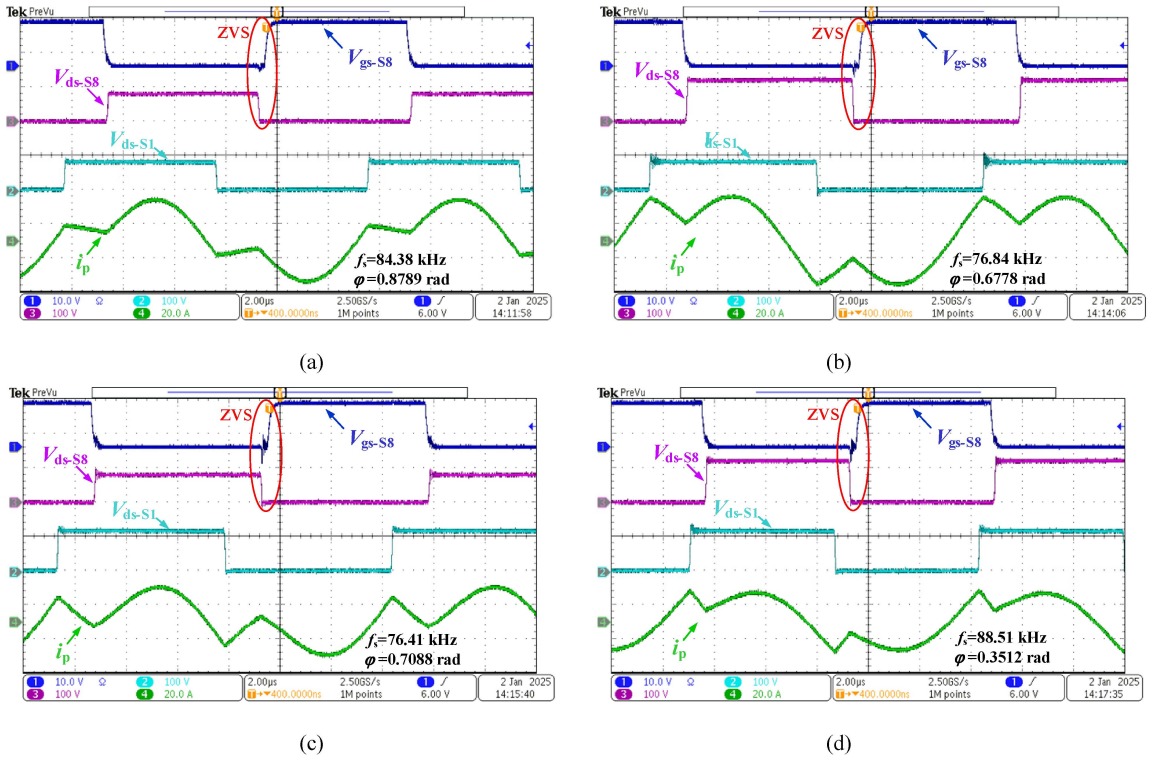

Fig. 24. ZVS realization of the secondary side switches at full load in the backward mode. (a) $V_{\mathrm{bus2}} = 80$ V, $V_{\mathrm{bus1}} = 80$ V. (b) $V_{\mathrm{bus2}} = 120$ V, $V_{\mathrm{bus1}} = 80$ V. (c) $V_{\mathrm{bus2}} = 80$ V, $V_{\mathrm{bus1}} = 120$ V. (d) $V_{\mathrm{bus2}} = 120$ V, $V_{\mathrm{bus1}} = 120$ V.

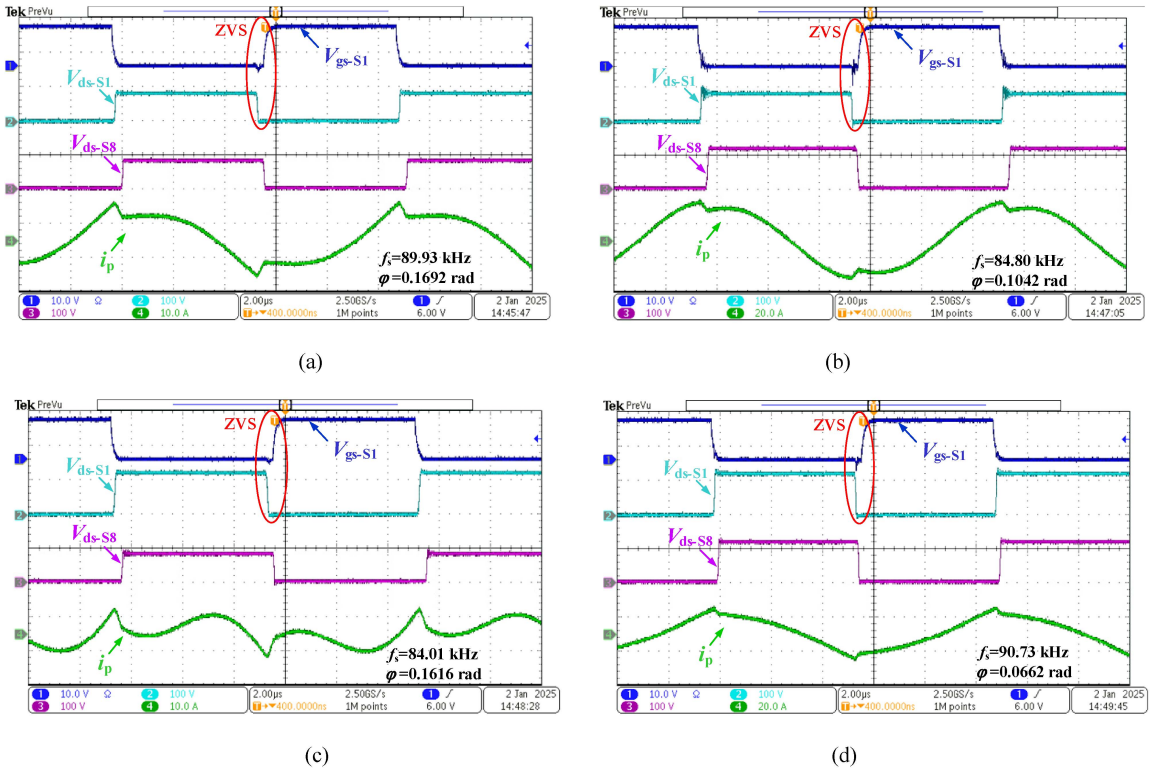

Fig. 25. ZVS realization of the primary side switches at 20% nominal load in the backward mode. (a) $V_{\mathrm{bus2}} = 80$ V, $V_{\mathrm{bus1}} = 80$ V. (b) $V_{\mathrm{bus2}} = 120$ V, $V_{\mathrm{bus1}} = 80$ V. (c) $V_{\mathrm{bus2}} = 80$ V, $V_{\mathrm{bus1}} = 120$ V. (d) $V_{\mathrm{bus2}} = 120$ V, $V_{\mathrm{bus1}} = 120$ V.

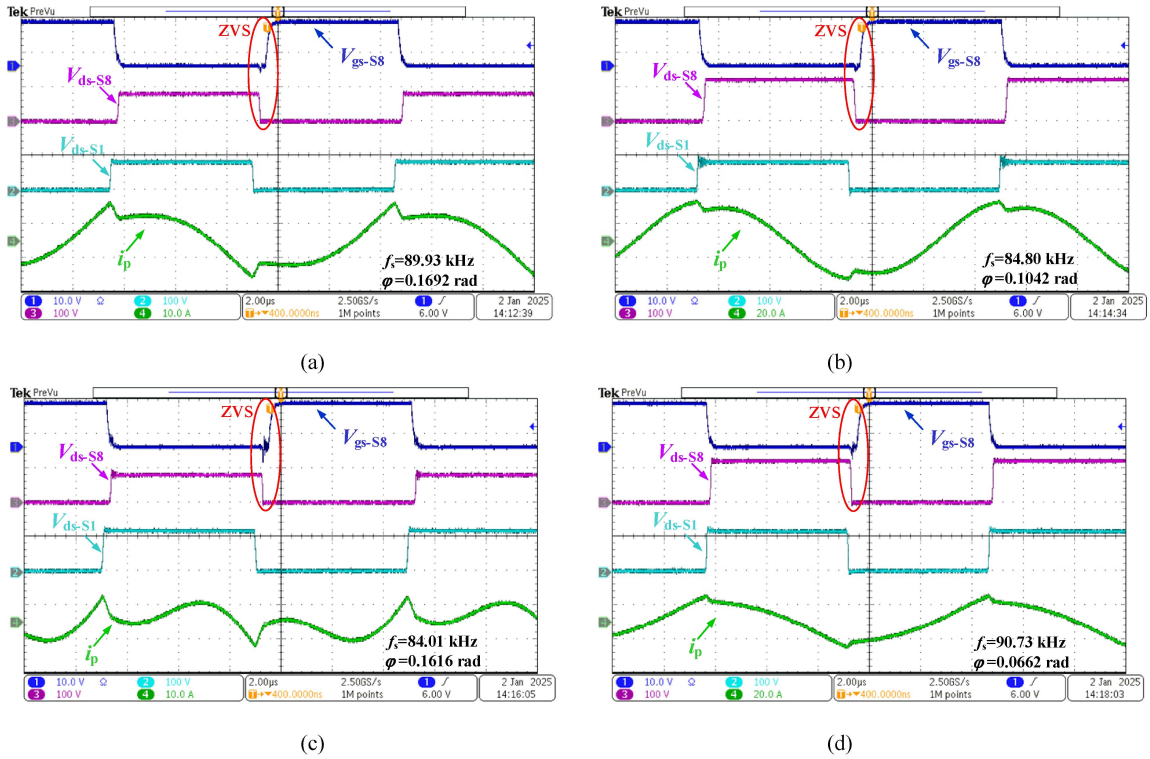

Fig. 26. ZVS realization of the secondary side switches at 20% nominal load in the backward mode. (a) $V_{\mathrm{bus2}} = 80$ V, $V_{\mathrm{bus1}} = 80$ V. (b) $V_{\mathrm{bus2}} = 120$ V , $V_{\mathrm{bus1}} = 80$ V. (c) $V_{\mathrm{bus2}} = 80$ V, $V_{\mathrm{bus1}} = 120$ V. (d) $V_{\mathrm{bus2}} = 120$ V, $V_{\mathrm{bus1}} = 120$ V.

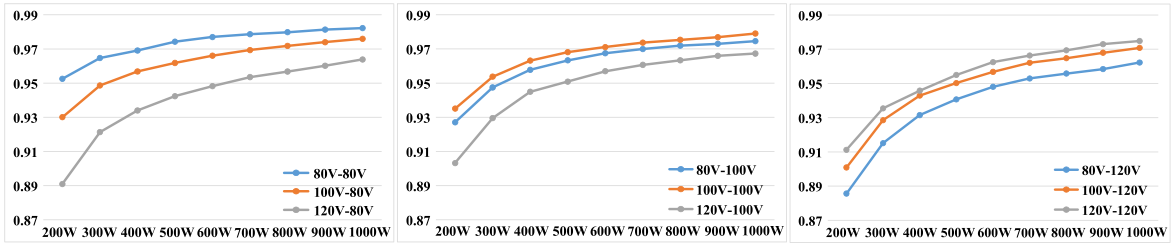

Fig. 27. Efficiency performance of the prototype in backward mode. (a) $V_{\mathrm{bus2}} = 80$ V–120 V, $V_{\mathrm{bus1}} = 80$ V. (b) $V_{\mathrm{bus2}} = 80$ V–120 V, $V_{\mathrm{bus1}} = 100$ V. (c) $V_{\mathrm{bus2}} = 80$ V–120 V, $V_{\mathrm{bus1}} = 120$ V.

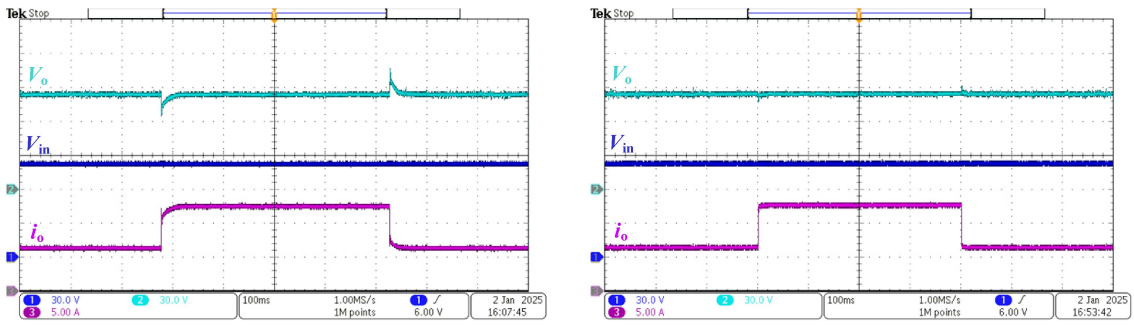

Fig. 28. 0% load step response in $V_{\mathrm{in}} = 80$ V, $V_{\mathrm{o}} = 80$ V. (a) PI control. (b) PI+ feedforward control.

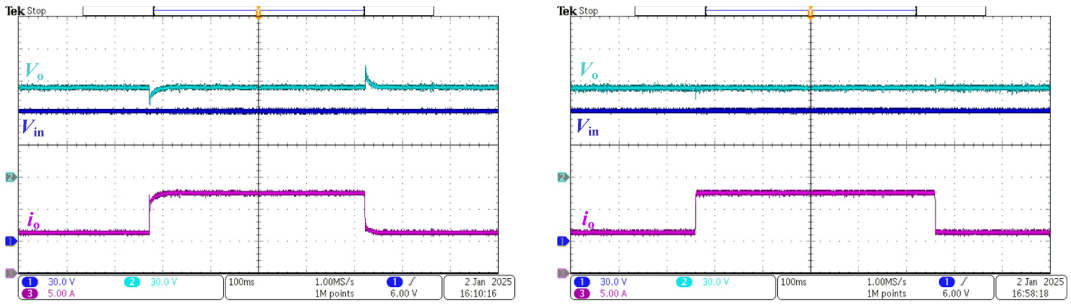

(a) (b)

Fig. 29. 50% load step response in $V_{\rm in} = 120$ V, $V_{\rm o} = 80$ V. (a) PI control. (b) PI + feedforward control.

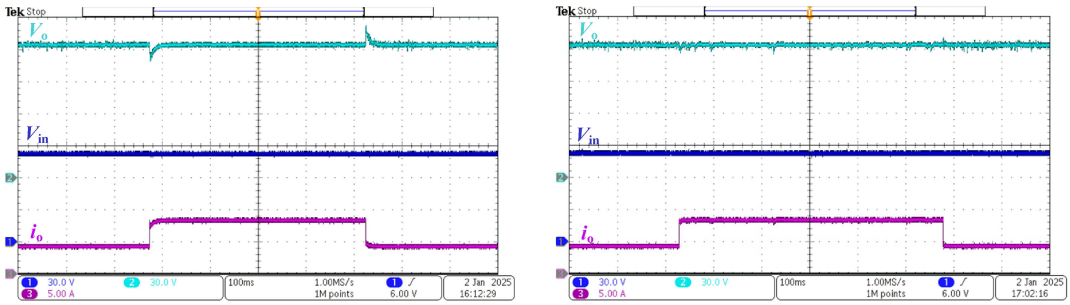

(a) (b)

Fig. 30. 50% load step response in $V_{\rm in} = 80$ V, $V_{\rm o} = 120$ V. (a) PI control. (b) PI + feedforward control.

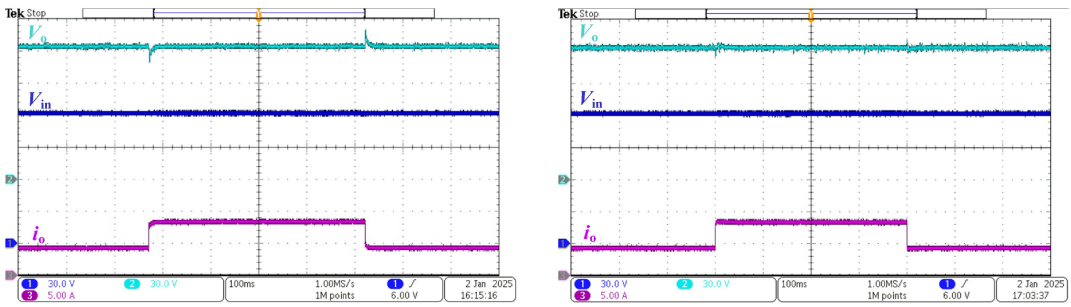

(a) (b)

Fig. 31. 50% load step response in $V_{\rm in} = 120$ V, $V_{\rm o} = 120$ V. (a) PI control. (b) PI + feedforward control.

2) Switching Frequency Range: In Table V, the converters can be divided into two types: the constant-frequency converter such as [34], [35], [39], [40] and the other type with variable switching frequency, such as [17], [18], [19], [29], [32], [41] and our prototype.

A constant switching frequency indeed facilitate the magnetic component design such as transformer and inductors. However, this is not conducive to covering a wide voltage range and improving the efficiency. Wu et al. [34], Huang et al. [35], Meinagh et al. [39], and Cheng et al. [40] proposed different control algorithms with constant switching frequency, which makes the design of magnetic components very convenient, however, the highest rated-power efficiency does not exceed 98%. Without the frequency as a control variable, the soft-switching range is hard to be enlarged so the efficiency performance is limited.

Resonant converters can obtain a good efficiency performance with VF control due to the soft-switching realization is much easier. In the range of VF converters, our proposed method shows the narrowest switching frequency range from 76.35 to 90.73 kHz, where the normalized value is 18.84% (= (90.73 kHz–76.35 kHz)/76.35 kHz). The other VF converters showed a much wider frequency range than the proposed method, for example, the normalized values of frequency range of [17], [18], [19], [29], [32], and [41] are, respectively, equal

TABLE V
PERFORMANCE COMPARISONS

Reference	[17]	[18]	[19]	[29]	[32]	[34]	[35]	[41]	[39]	[40]	Proposed
Converter topology	*CLLC*	*CLLC*	*LLC-C*	*LLC-L*	*LLC-L*	*LLC-L*	Coupled inductor-C	*CLLC*	*CLLC*	*CLLC*	*LLC-C*
Rated power P_N	1 kW	1.2 kW	1 kW	1 kW	1 kW	1.6 kW	1 kW	500 W	1 kW	800 W	1 kW
Bidirectional Normalized Gain Range (input range × output range)	1 × 1.353	1 × 1.375	1 × 1.8	1.5 × 1	1.5 × 1.5	1.5 × 1	1 × 1.667	1	1	1 × 1.5	1.5 × 1.5
Vin (V) Vout (V) (forward mode)	200 170–230	380 160–220	400 250–450	80–120 400	80–120 80–120	320–480 400	400 300–500	100 100	400 360	400 320–480	80–120 80–120
Vin (V) Vout (V) (backward mode)	170–230 200	160–220 380	250–450 400	400 80–120	80–120 80–120	400 320–480	300–500 400	100 100	Not reported	Not reported	80–120 80–120
Modulation type	VF	VF+PS	VF	VF	VF+SPS	PWM	PWM	VF+SPS	TPS	TPS	VF+SPS
Switching frequency variation range $(f_{s\_max}-f_{s\_min})/f_{s\_min}$	173% 55 kHz–150 kHz	275% 80 kHz–300 kHz	300% 50 kHz–200 kHz	33.33% 69 kHz–92 kHz	22.6% 89.2 kHz–109.4 kHz	0% 100 kHz	0% 250 kHz	24.4% 41 kHz–51 kHz	0% 100 kHz	0% 160 kHz	18.84% 76.35 kHz–90.73 kHz
Minimum number of inductor, transformer and resonant capacitor	2L+1T+2C	2L+1T+2C	1L+1T+2C	2L+1T+1C	2L+1T+1C	2L+1T+1C	1T(Coupled inductor)+4C	2L+1T+2C	2L+1T+2C	2L+1T+2C	1L+1T+2C
Core saturation risk	No	No	No	Yes	Yes	Yes	No	No	No	No	No
Highest rated-power efficiency (forward mode)	97.1%	98.07%	98.3%	96.2%	97.5%	97.8%	96.4%	93.6%	96%	96.1%	98.10%
Load range in efficiency curve (forward mode)	100%	10%–100%	25%–100%	20%–100%	20%–100%	12.5%–100%	10%–100%	20%–100%	10%–100%	10%–100%	20%–100%
Highest rated-power efficiency (backward mode)	97.1%	Reported similar as forward	98.4%	96%	Not reported	97.8%	96.6%	92.8%	Not reported	Not reported	98.24%
Load range in efficiency curve (backward mode)	100%	Reported similar as forward	50%–100%	20%–100%	Not reported	12.5%–100%	10%–100%	20%–100%	Not reported	Not reported	20%–100%

to 173%, 275%, 300%, 33.33%, 22.6%, and 24.4%, which are all above 20%.

3) Voltage Ranges in Both Ports of the Converter: Most designs are only suitable for the situation that the port voltage changes at one side but the other port voltage must keep constant. Different from that, our proposed design method can cover a wide voltage range for both ports of the converter in any power flow directions. When taking the voltage ranges of the two ports into account, our prototype shows the widest voltage range, where the normalized voltage range is 2.25 (= (120 V/80)×(120 V/80)). Although [32] can cover the same voltage ranges, the proposed method can achieve a higher efficiency and a narrower switching frequency range. Moreover, there is no core saturation risk in our prototype as mentioned above.

4) Efficiency: In Table V, only [18] (98.07%), [19] (98.4%), and our prototype (98.24%) can achieve that the highest rated-power efficiency exceeds 98%. However, Li et al. [18] and Zhao et al. [19] both showed a very wide switching frequency range: the switching frequency range of [18] is from 80–300 kHz and it ranges from 50–200 kHz in [19]. For our prototype, the frequency changes only from 76.35 to 90.73 kHz.

Moreover, it should be noted that the selection of main circuit parameter in [19] mainly focused on the forward operation mode. When the converter operates in reverse mode, most of the operating conditions need to be achieved in a step-down mode, which means it needs a very high switching frequency to regulate the output when the output power gradually decreases. Therefore, in its preset frequency range (50–200 kHz), it cannot operate in reverse mode below 50% of the rated power. Similarly, the bidirectional voltage gain range of [18] is smaller than the proposed method due to the restriction of the parameter design in a *CLLC* resonant converter. Hence, although the highest rated-power efficiency is similar, our prototype shows a wider load range and voltage range compared with [18] and [19].

5) Minimum Component Number of the Resonant Tank: The magnetic component always takes up a big volume so the minimum component number of resonant tank is also compared in Table V.

It can be proved that *LLC-C* can be totally equivalent to the *CLLC* tank even with a less inductor number [20], [21]. Hence, a prototype can be built by the *LLC-C* tank after the parameters for a *CLLC* tank have been determined (see Appendix B). Since the necessary component number for the *LLC-C* resonant tank

is only equal to 4 (= 1 inductor, 1 transformer, and 2 resonant capacitors), it shows a good superior in Table V.

VII. Conclusion

A circuit parameter design method and a VF&SPS control strategy are proposed for the *CLLC* RDAB converter. Based on the analysis about the gain model and the soft-switching region, the frequency range of $f_n \in (X_3, 1)$, which is suitable for the VF&SPS control strategy and the realization of soft-switching, is proposed. Furthermore, a function between the two control variables is also proposed, which is a linear function with adjustable slope (K_m) and intercept (B_m) according to the voltage gain. By this method, the converter can be operated close to the boundary of the ZVS region so as to realize a small switching-OFF current value. Moreover, a feedforward control algorithm is proposed, which using a curve fitting method in order to calculate the approximate value of the control variable, so that this value can be added into the control loop to improve the load-step response. Finally, a 1 kW prototype is built to verify the correctness of the theoretical analysis. With the parameter equivalent method, the *CLLC* resonant tank is realized by an *LLC-C* tank so to reduce one inductor and improve the power density. The experimental results show that all switches can achieve the soft-switching with a wide voltage range and a wide load range. The maximum rated-power efficiencies of the forward and backward modes are 98.10% and 98.24%, respectively. In addition, the switching frequency in the whole operating range only changes 18.84%, which decreases the difficulty for the design of the transformer.

Appendix A

Here is a derivation process for the normalized gain in forward mode.

By Kirchhoff's voltage law, (A1) can be obtained according to (3)–(6)

$$\begin{bmatrix} V_{AB1}e^{-\varphi j} \\ n_5 V_{CD1}e^{0j} \end{bmatrix} = \begin{bmatrix} R_0 f_n + kR_0 f_n - \frac{R_0}{f_n} & -kR_0 f_n \\ kR_0 f_n & \frac{R_0}{f_n} - R_0 f_n - kR_0 f_n \end{bmatrix} \times \begin{bmatrix} I_p e^{(\frac{\pi}{2}-\varphi-\theta_1)j} \\ \frac{I_s}{n_5} e^{(\frac{\pi}{2}+\theta_2)j} \end{bmatrix} \tag{A1}$$

where f_r, R_0, f_n, and k, respectively, denote the resonant frequency, the characteristic impedance, the normalized frequency, and the inductor ratio, defined as

$$f_r = \frac{1}{2\pi\sqrt{L_a C_a}} \tag{A2}$$

$$R_0 = \sqrt{\frac{L_a}{C_a}} \tag{A3}$$

$$f_n = \frac{f_s}{f_r} \tag{A4}$$

$$k = \frac{L_b}{L_a}. \tag{A5}$$

The coefficient matrix of (A1) is defined as A for simplicity and given in (A6). The determinant of A is given in (A7)

$$\boldsymbol{A} = \begin{bmatrix} R_0 f_n + kR_0 f_n - \frac{R_0}{f_n} & -kR_0 f_n \\ kR_0 f_n & \frac{R_0}{f_n} - R_0 f_n - kR_0 f_n \end{bmatrix} \tag{A6}$$

$$|\boldsymbol{A}| = kR_0{}^2 f_n \left(\frac{1}{f_n} - f_n\right)\left(2 + \frac{1}{k} - \frac{1}{kf_n{}^2}\right). \tag{A7}$$

The current and phase angle are not unique solution in (A1) when $|A|$ is equal to 0. This case should be avoided. With the assumption of $|A| \neq 0$, (A1) can be simplified to

$$\begin{bmatrix} I_p e^{(\frac{\pi}{2}-\varphi-\theta_1)j} \\ \frac{I_s}{n_5} e^{(\frac{\pi}{2}+\theta_2)j} \end{bmatrix} = \frac{kR_0 f_n}{|A|} \begin{bmatrix} \frac{1}{kf_n{}^2} - \frac{1}{k} - 1 & 1 \\ -1 & 1 + \frac{1}{k} - \frac{1}{kf_n{}^2} \end{bmatrix} \times \begin{bmatrix} V_{AB1}e^{-\varphi j} \\ n_5 V_{CD1}e^{0j} \end{bmatrix}. \tag{A8}$$

According to Euler's formula, (A8) can be expanded, as shown in

$$\begin{cases} I_p \cos\theta = \frac{kR_0 f_n}{|A|} n_5 V_{CD1} \sin\varphi_1 \\ I_p \sin\theta_1 = \frac{kR_0 f_n}{|A|} n_5 V_{CD1} \cos\varphi \\ \qquad\quad - \frac{kR_0 f_n}{|A|}\left(1 + \frac{1}{k} - \frac{1}{kf_n{}^2}\right) V_{AB1} \\ \frac{I_s}{n_5} \cos\theta_2 = \frac{kR_0 f_n}{|A|} V_{AB1} \sin\varphi \\ \frac{I_s}{n_5} \sin\theta_2 = \frac{kR_0 f_n}{|A|} V_{AB1} \cos\varphi \\ \qquad\quad - \frac{kR_0 f_n}{|A|}\left(1 + \frac{1}{k} - \frac{1}{kf_n{}^2}\right) n_5 V_{CD1}. \end{cases} \tag{A9–A12}$$

By solving (A9)–(A12), the current amplitude and the phase angles can be solved, as shown in

$$I_p = \frac{4}{\pi}\sqrt{\frac{n_5{}^2 V_{bus2}^2 + \left(1 + \frac{1}{k} - \frac{1}{kf_n{}^2}\right)^2 V_{bus1}^2 - 2V_{bus1} n_5 V_{bus2} \cos\varphi \left(1 + \frac{1}{k} - \frac{1}{kf_n{}^2}\right)}{R_0\left[\left(\frac{1}{f_n} - f_n\right)\left(2 + \frac{1}{k} - \frac{1}{kf_n{}^2}\right)\right]}} \tag{A13}$$

$$I_s = \frac{4n_5}{\pi}\sqrt{\frac{V_{bus1}^2 + \left(1 + \frac{1}{k} - \frac{1}{kf_n{}^2}\right)^2 n_5{}^2 V_{bus2}^2 - 2V_{bus1} n_5 V_{bus2} \cos\varphi \left(1 + \frac{1}{k} - \frac{1}{kf_n{}^2}\right)}{R_0\left[\left(\frac{1}{f_n} - f_n\right)\left(2 + \frac{1}{k} - \frac{1}{kf_n{}^2}\right)\right]}} \tag{A14}$$

$$\theta_1 = \arctan\left(\frac{1}{\tan\varphi} - \frac{1 + \frac{1}{k} - \frac{1}{kf_n{}^2}}{\sin\varphi}\frac{V_{bus1}}{n_5 V_{bus2}}\right) \tag{A15}$$

$$\theta_2 = \arctan\left(\frac{1}{\tan\varphi} - \frac{1 + \frac{1}{k} - \frac{1}{kf_n{}^2}}{\sin\varphi} \times \frac{n_5 V_{bus2}}{V_{bus1}}\right). \tag{A16}$$

According to the energy conservation law, (A17) can be obtained, and finally, the normalized gain can be derived, as shown in (7) for the forward operation mode

$$\frac{T_s}{2}\frac{V_{AB1}}{\sqrt{2}}\frac{I_p}{\sqrt{2}}\cos\theta_1 = \frac{T_s}{2}\frac{V_{bus2}^2}{R_L}. \tag{A17}$$

APPENDIX B

Compared with the *CLLC* converter, the *LLC-C* resonant converter, as shown in Fig. 1(c), can achieve the same features with proper parameters. Zahid et al. [20] and Tan and Ruan [21] indicated that *CLLC* converter can be equivalent to the *LLC-C* converter with the parameter relationship shown in

$$\begin{cases} n_4 = \frac{n_5 L_{\mathrm{b}}}{{n_5}^2 L_{\mathrm{c}} + L_{\mathrm{b}}} \\ L_{\mathrm{m}} = \frac{{L_{\mathrm{b}}}^2}{{n_5}^2 L_{\mathrm{c}} + L_{\mathrm{b}}} \\ L_{\mathrm{r}} = L_{\mathrm{a}} + L_{\mathrm{b}} - \frac{{L_{\mathrm{b}}}^2}{{n_5}^2 L_{\mathrm{c}} + L_{\mathrm{b}}}. \\ C_{\mathrm{r1}} = C_{\mathrm{a}}, C_{\mathrm{r2}} = C_{\mathrm{b}} \end{cases} \quad \text{(A18)–(A22)}$$

REFERENCES

[1] Y. Xuan, X. Yang, W. Chen, T. Liu, and X. Hao, "A novel three-level CLLC resonant DC-DC converter for bidirectional EV charger in DC microgrids," *IEEE Trans. Ind. Electron.*, vol. 68, no. 3, pp. 2334–2344, Mar. 2021.

[2] B. L. Narasimharaju, V. V. Prahlad, U. R. Reddy, K. Vijay Babu, and P. Srinivasan, "Optimized dual active bridge Bi-directional DC-DC converter for UPS application," in *Proc. IEEE Int. Conf. Power Electron., Drives Energy Syst.*, 2014, pp. 1–6.

[3] R. T. Naayagi, A. J. Forsyth, and R. Shuttleworth, "High-power bidirectional DC-DC converter for aerospace applications," *IEEE Trans. Power Electron.*, vol. 27, no. 11, pp. 4366–4379, Nov. 2012.

[4] K. - H. Chao and C. - H. Huang, "Bidirectional DC-DC soft-switching converter for stand-alone photovoltaic power generation systems," *IET Power Electron.*, vol. 7, pp. 1557–1565, 2014.

[5] J. Zeng, X. Du, and Z. Yang, "A multiport bidirectional DC-DC converter for hybrid renewable energy system integration," *IEEE Trans. Power Electron.*, vol. 36, no. 11, pp. 12281–12291, Nov. 2021.

[6] L. Cao, K. H. Loo, and Y. M. Lai, "Output-impedance shaping of bidirectional DAB DC–DC converter using double-proportional-integral feedback for near-ripple-free DC bus voltage regulation in renewable energy systems," *IEEE Trans. Power Electron.*, vol. 31, no. 3, pp. 2187–2199, Mar. 2016.

[7] X. Fang, H. Hu, Z. J. Shen, and I. Batarseh, "Operation mode analysis and peak gain approximation of the LLC resonant converter," *IEEE Trans. Power Electron.*, vol. 27, no. 4, pp. 1985–1995, Apr. 2012.

[8] X. Fang et al., "Efficiency-oriented optimal design of the LLC resonant converter based on peak gain placement," *IEEE Trans. Power Electron.*, vol. 28, no. 5, pp. 2285–2296, May 2013.

[9] Z. Fang, T. Cai, S. Duan, and C. Chen, "Optimal design methodology for LLC resonant converter in battery charging applications based on time-weighted average efficiency," *IEEE Trans. Power Electron.*, vol. 30, no. 10, pp. 5469–5483, Oct. 2015.

[10] H. Huang, "Designing an LLC resonant half-bridge power converter," Texas Instruments, Dallas, TX, USA, Tech. Rep. SLUP263, 2010.

[11] H. Li, Z. Zhang, S. Wang, J. Tang, X. Ren, and Q. Chen, "A 300-kHz 6.6-kW SiC bidirectional LLC onboard charger," *IEEE Trans. Ind. Electron.*, vol. 67, no. 2, pp. 1435–1445, Feb. 2020.

[12] V. K. Jaiswal and A. Ghoshal, "A design methodology of bidirectional LLC resonant converter for energy storage systems," in *Proc. IEEE Transp. Electrific. Conf. Expo, Asia-Pacific*, Seogwipo, South Korea, 2019, pp. 1–6.

[13] X. Zhou, C. Chen, K. Ni, H. Mi, J. Yang, and T. Yang, "A parameter design method for L-LLC resonant converter," in *Proc. IEEE 2nd Int. Power Electron. Appl. Symp.*, Guangzhou, China, 2023, pp. 1205–1210.

[14] J. -H. Jung, H. -S. Kim, M. -H. Ryu, and J. -W. Baek, "Design methodology of bidirectional CLLC resonant converter for high-frequency isolation of DC distribution systems," *IEEE Trans. Power Electron.*, vol. 28, no. 4, pp. 1741–1755, Apr. 2013.

[15] P. He, A. Mallik, A. Sankar, and A. Khaligh, "Design of a 1-MHz high-efficiency high-power-density bidirectional GaN-based CLLC converter for electric vehicles," *IEEE Trans. Veh. Technol.*, vol. 68, no. 1, pp. 213–223, Jan. 2019.

[16] J. Min and M. Ordonez, "Bidirectional resonant CLLC charger for wide battery voltage range: Asymmetric parameters methodology," *IEEE Trans. Power Electron.*, vol. 36, no. 6, pp. 6662–6673, Jun. 2021.

[17] R. Wei, L. Ding, R. Liu, and Y. Li, "An intuitive and noniterative design methodology for CLLC chargers employing simplified operation modes model," *IEEE Trans. Power Electron.*, vol. 38, no. 6, pp. 7771–7784, Jun. 2023.

[18] B. Li, M. Chen, X. Sun, J. Wang, and F. Jiang, "A hybrid control for smooth power direction transition of bidirectional resonant CLLC converter with wide voltage gain," *IEEE Trans. Power Electron.*, vol. 39, no. 12, pp. 15898–15914, Dec. 2024.

[19] L. Zhao, Y. Pei, L. Wang, L. Pei, W. Cao, and Y. Gan, "Design methodology of bidirectional resonant CLLC charger for wide voltage range based on parameter equivalent and time domain model," *IEEE Trans. Power Electron.*, vol. 37, no. 10, pp. 12041–12064, Oct. 2022.

[20] Z. U. Zahid, Z. M. Dalala, R. Chen, B. Chen, and J. -S. Lai, "Design of bidirectional DC–DC resonant converter for vehicle-to-grid (V2G) applications," *IEEE Trans. Transp. Electrific.*, vol. 1, no. 3, pp. 232–244, Oct. 2015.

[21] X. Tan and X. Ruan, "Equivalence relations of resonant tanks: A new perspective for selection and design of resonant converters," *IEEE Trans. Ind. Electron.*, vol. 63, no. 4, pp. 2111–2123, Apr. 2016.

[22] W. Chen, P. Rong, and Z. Lu, "Snubberless bidirectional DC–DC converter with new CLLC resonant tank featuring minimized switching loss," *IEEE Trans. Ind. Electron.*, vol. 57, no. 9, pp. 3075–3086, Sep. 2010.

[23] A. V. Mirtchev and E. C. Tatakis, "Design methodology based on dual control of a resonant dual active bridge converter for electric vehicle battery charging," *IEEE Trans. Veh. Technol.*, vol. 71, no. 3, pp. 2691–2705, Mar. 2022.

[24] S. Zou, J. Lu, A. Mallik, and A. Khaligh, "Bi-directional CLLC converter with synchronous rectification for plug-in electric vehicles," *IEEE Trans. Ind. Appl.*, vol. 54, no. 2, pp. 998–1005, Mar./Apr. 2018.

[25] X. Li, J. Huang, Y. Ma, X. Wang, J. Yang, and X. Wu, "Unified modeling, analysis, and design of isolated bidirectional CLLC resonant DC–DC converters," *IEEE J. Emerg. Sel. Topics Power Electron.*, vol. 10, no. 2, pp. 2305–2318, Apr. 2022.

[26] B. Li, M. Chen, X. Wang, N. Chen, X. Sun, and D. Zhang, "An optimized digital synchronous rectification scheme based on time-domain model of resonant CLLC circuit," *IEEE Trans. Power Electron.*, vol. 36, no. 9, pp. 10933–10948, Sep. 2021.

[27] Y. Wang, F. Wang, F. Zhuo, J. Tian, K. Yu, and R. Song, "Synchronous rectification strategy of CLLC resonant converter based on accurate time-domain model," *IEEE J. Emerg. Sel. Topics Power Electron.*, vol. 12, no. 1, pp. 516–530, Feb. 2024.

[28] H. Chen, K. Sun, H. Shi, J. -I. Ha, and S. Lee, "A battery charging method with natural synchronous rectification features for full-bridge CLLC converters," *IEEE Trans. Power Electron.*, vol. 37, no. 2, pp. 2139–2151, Feb. 2022.

[29] T. Jiang, J. Zhang, X. Wu, K. Sheng, and Y. Wang, "A bidirectional LLC resonant converter with automatic forward and backward mode transition," *IEEE Trans. Power Electron.*, vol. 30, no. 2, pp. 757–770, Feb. 2015.

[30] J. Liu, Y. Ai, S. Chen, Z. Zhang, and Y. Shi, "A hybrid pulse frequency modulation control strategy for L-LLC resonant converter," *IEEE J. Emerg. Sel. Topics Power Electron.*, vol. 10, no. 6, pp. 6960–6972, Dec. 2022.

[31] T. Jiang, X. Chen, J. Zhang, and Y. Wang, "Bidirectional LLC resonant converter for energy storage applications," in *Proc. 28th Annu. IEEE Appl. Power Electron. Conf. Expo.*, 2013, pp. 1145–1151.

[32] P. Jia, T. Guo, X. Zhu, and T. Shao, "A control strategy for the bidirectional LLC-L converter to extend the gain range based on the time domain analytical model," *IEEE Trans. Power Electron.*, vol. 38, no. 4, pp. 4876–4893, Apr. 2023.

[33] P. Jia, K. Qiu, M. Liang, T. Shao, and Y. Zhang, "A simple variable frequency and single-phase-shifted control for the dual active bridge series resonant converter," *IEEE J. Emerg. Sel. Topics Ind. Electron.*, vol. 6, no. 1, pp. 308–326, Jan. 2025.

[34] H. Wu, S. Ding, K. Sun, L. Zhang, Y. Li, and Y. Xing, "Bidirectional soft-switching series-resonant converter with simple PWM control and load-independent voltage-gain characteristics for energy storage system in DC microgrids," *IEEE J. Emerg. Sel. Topics Power Electron.*, vol. 5, no. 3, pp. 995–1007, Sep. 2017.

[35] J. Huang, H. Han, G. Xu, X. Liu, W. Xiong, and M. Su, "Coupled-inductor-based bidirectional resonant converter with reduced component count and load-independent voltage gain," *IEEE Trans. Ind. Electron.*, vol. 71, no. 2, pp. 1559–1571, Feb. 2024.

[36] W. Han, R. Mal, and L. Corradini, "Analysis and design methodology for ZVS phase shift modulated bidirectional CLLLC resonant DC-DC converters," in *Proc. 21st Eur. Conf. Power Electron. Appl.*, 2019, pp. P.1–P.10.

[37] R. P. Twiname, D. J. Thrimawithana, U. K. Madawala, and C. A. Baguley, "A dual-active bridge topology with a tuned CLC network," *IEEE Trans. Power Electron.*, vol. 30, no. 12, pp. 6543–6550, Dec. 2015.
[38] W. L. Malan, D. M. Vilathgamuwa, and G. R. Walker, "Modeling and control of a resonant dual active bridge with a tuned CLLC network," *IEEE Trans. Power Electron.*, vol. 31, no. 10, pp. 7297–7310, Oct. 2016.
[39] F. A. A. Meinagh, J. Min, M. Ordonez, M. Craciun, and C. Botting, "Improved triple-phase-shift modulation for bidirectional CLLC converters," *IEEE Trans. Power Electron.*, vol. 38, no. 6, pp. 7348–7361, Jun. 2023.
[40] Z. Cheng, L. He, and H. Zhou, "Optimal triple-phase-shift modulation strategy for wide-gain high-efficiency bidirectional CLLC converter," *IEEE Trans. Transp. Electrific.*, to be published, doi: 10.1109/TTE.2024.3491974.
[41] T. Mishima and Y. Koga, "Variable frequency phase-difference controlled CLLC resonant bidirectional DC-DC converter featuring wide-range ZVS performance and reactive power reduction," in *Proc. IEEE Energy Convers. Congr. Expo.*, 2018, pp. 6283–6290.

Pengyu Jia (Member, IEEE) was born in Hebei Province, China, in 1985. He received the B.S. and Ph.D. degrees in electrical engineering from Beijing Jiaotong University, Beijing, China, in 2008 and 2014, respectively.

He is currently with the School of Electrical and Control Engineering, North China University of Technology. His current research interests include modeling of dc–dc converter and the corresponding control methods.

Yiheng Zhang (Student Member, IEEE) was born in Sichuan Province, China, in 1999. He received the B.S. degree in electrical engineering from Sichuan University of Science and Engineering, Zigong, China, in 2021. He is currently working toward the master's degree in electrical engineering with the School of Electrical and Control Engineering, North China University of Technology, Beijing, China.

His current research interests include the modeling of converter and the control strategy of dc–dc converters.

Mingjun Liu (Student Member, IEEE) was born in Shandong Province, China, in 1999. He received the B.S. degree in electrical engineering and automation from Shandong University of Technology, Zibo, China. in 2022. He is currently working toward the master's degree in electrical engineering with the School of Electrical and Control Engineering, North China University of Technology, Beijing, China.

His current research interests include the topology derivation and control strategy of dc–dc converter.

Yimei Xing (Student Member, IEEE) was born in Henan Province, China, in 1999. She received the B.S. degree in electrical engineering from College of Zhengzhou University of Aeronautics, Zhengzhou, China, in 2022. She is currently working toward the master's degree in electrical engineering with the School of Electrical and Control Engineering, North China University of Technology, Beijing, China.

Her current research interest includes control strategy of dc–dc converter.